

Spurious dianeutral mixing and the role of momentum closure

Mehmet Ilıcak^{a,*}, Alistair J. Adcroft^a, Stephen M. Griffies^b and Robert W. Hallberg^b

^a*Atmospheric and Oceanic Sciences Program, Princeton University, Princeton, NJ 08540, USA*

^b*NOAA-GFDL, Princeton University, Forrestal Campus, 201 Forrestal Road, Princeton, NJ 08542, USA*

Abstract

This paper examines spurious dianeutral transport within a suite of ocean models (GOLD, MITGCM, MOM, and ROMS). We quantify such transport through a global diagnostic that computes the reference potential energy, whose evolution arises solely through transport between density classes. Previous studies have focused on the importance of accurate tracer advection schemes in reducing the spurious transport and closure. The present study highlights complementary issues associated with momentum transport. Spurious dianeutral transport is shown to be directly proportional to the lateral grid Reynolds number (Re_{Δ}), with such transport significantly reduced when $Re_{\Delta} < 10$.

Simulations with the isopycnal model GOLD provide a benchmark for the smallest level of spurious dianeutral transport realizable in our model suite. For idealized simulations with a linear equation of state, GOLD exhibits identically zero spurious dianeutral mixing, and thus maintains a constant reference potential energy when all physical mixing processes are omitted. Amongst the non-isopycnal models tested in idealized simulations, ROMS generally produces smaller spurious dianeutral mixing than MITGCM or MOM, since ROMS makes use of a higher order upwind-biased scheme for momentum transport that enforces a small Re_{Δ} . In contrast, MITGCM and MOM both employ unbiased (centered) discretizations of momentum transport, and therefore rely on lateral friction operators to control the grid Reynolds number. We find that a lateral shear-dependent Smagorinsky viscosity provides an effective means to locally reduce Re_{Δ} , and thus to reduce spurious dianeutral transport in MITGCM and MOM.

In addition to four idealized simulations, we quantify spurious dianeutral transport in realistic global ocean climate simulations using GOLD and MOM with a realistic equation of state for seawater, both with and without mesoscale eddies in the resolved flow field. The GOLD simulations have detectable levels of spurious cabbeling from along isopycnal advective truncation errors. Significantly larger spurious dianeutral transport arises in a non-eddying MOM simulation. In an eddying MOM simulation, spurious dianeutral transport is larger still but is reduced by increasing momentum friction.

Key words: Spurious dianeutral transport; cabbeling, overflows; exchange-flow; ocean models; momentum transport; tracer advection; reference potential energy

1. Introduction

This paper examines the issues of spurious dianeutral mixing in numerical models of ocean circulation. We update the study of Griffies et al. (2000) who concluded that the state-of-the-science tracer advection schemes then available for geopotential

* Corresponding author. Mehmet Ilıcak. NOAA-GFDL, Princeton University, Forrestal Campus, 201 Forrestal Road, Princeton, NJ 08542, USA

Email address: mehmet.ilicak@noaa.gov (Mehmet Ilıcak).

coordinate ocean models could lead to unphysically large levels of spurious diapycnal mixing, especially in the presence of mesoscale eddies. The present paper emphasizes the critical importance of *both* tracer and momentum transport methods.

The large scale circulation of the ocean is primarily driven by momentum and buoyancy fluxes through the upper and lower boundaries, but turbulent mixing is required to maintain that circulation in conjunction with stratification (Munk and Wunsch, 1998). There are regions of vigorous mixing, particularly in the upper and lower boundary layers (e.g. Large et al. (1994); Legg et al. (2009)), above rough topography (e.g. Kunze and Sanford (1996); Kunze et al. (2006)), and in regions of high shears such as the Equatorial undercurrent. In contrast, turbulent mixing has been observed to be very weak in much of the ocean (e.g. Ledwell et al., 1993; Gregg et al., 2003; Ledwell et al., 2011)). Both epineutral (along density) and diapycnal mixing modify water properties, but diapycnal mixing is thought to be the most important mechanism for modifying water mass densities. Cabelling and thermobaricity, processes arising from the nonlinearity of the equation of state for seawater (McDougall, 1987; IOC et al., 2010), also contribute to diapycnal transport, especially in the Southern Ocean (Marsh, 2000; Iudicone et al., 2008; Klocker and McDougall, 2010).

Modern numerical models of the global ocean try to appropriately represent the dynamic and geographic variation of turbulent mixing through a variety of sub-grid scale parameterizations (e.g. Large et al. (1994); Simmons et al. (2004); Jackson et al. (2008)). However, Griffies et al. (2000) recognized that numerical models, especially non-isopycnal coordinate models, also exhibit spurious mixing that arises from truncation errors in the discrete advection schemes used for ostensibly conserved quantities. They quantified spurious mixing in idealized basin scale simulations and suggested that it may be significant for large scale ocean climate.

The main motivation to understand and reduce spurious diapycnal transport is due to the need to retain water masses over basin scales for timescales of decades to centuries, or hundreds of eddy turnover times. This is an extremely difficult numerical transport problem, especially in non-isopycnal-coordinate models. In addition to degrading water mass integrity, spurious diapycnal transport introduces a spurious source for poten-

tial energy. As more understanding of the ocean's energy cycle unfolds (Munk and Wunsch, 1998; Wunsch and Ferrari, 2004), respecting this cycle in ocean models provides a useful means for evaluating the integrity of ocean climate simulations.

Griffies et al. (2000) noted that spurious mixing was a function of resolution and became larger for eddy-permitting simulations, because of the tendency for geostrophic turbulence to strain large scale tracer gradients, thereby enhancing tracer variance at the grid scale (numerical advection schemes tend to "disperse" grid-scale noise). They also recommended that to minimize spurious diapycnal mixing, boundary currents must be resolved with no less than roughly two grid points. Subsequent to Griffies et al. (2000), an implicit assumption has been that improvement in the tracer advection schemes is needed. For example, Marchesiello et al. (2009) propose a modification of a third order scheme designed to rotate the diffusive component of the numerical transport to minimize the diapycnal projection. However, we will show here that an appropriate level of viscous dissipation is also important to control spurious mixing.

There are various methods that have been used to diagnose spurious mixing in ocean models. Griffies et al. (2000) employed a sorting approach which led to an isopycnally averaged effective diapycnal diffusivity. Such a diffusivity-based diagnostic approach was also pursued by Getzlaff et al. (2010) and Hill et al. (2011). We highlight two limitations with this approach.

- (i) A diagnosed diapycnal diffusivity is very noisy, since it is subject to divisions by small numbers. Some form of filtering or layer averaging is therefore required to produce robust diffusivities.
- (ii) The diagnosed spurious diapycnal diffusivity is not always meaningful, as the following example illustrates. Two geographically separate water parcels of similar potential density will appear next to each other in a sorted density profile. A change in volume of one of those parcels, say due to mixing with a third parcel, will appear as mixing between the first two parcels. Such apparent mixing does not actually occur in the unsorted system, since the parcels are physically unconnected.

There have also been attempts to use passive tracers to diagnose spurious mixing. Passive tracer

release simulations provide useful geographical information about mixing (Getzlaff et al., 2010; Hill et al., 2011). However, the diagnosed spurious diffusivity is dependent on the structure of the tracer concentration. Although tracer release experiments yield potentially meaningful diffusivities for heat and salt in the real ocean, a numerical tracer release (especially with a local extrema) will reveal large diffusivities that may not affect the temperature and salinity fields (for instance, in a smoothly stratified ocean).

An alternative approach was suggested by Burchard and Rennau (2008), based on the variance decay of individual tracers. This method has the appeal of diagnosing a three-dimensional effective diffusivity, thus providing three-dimensional information about spurious mixing. Unfortunately, this method does not distinguish between dianeutral and epineutral mixing, a distinction that matters to the questions being addressed in the present study. Finally, Lee et al. (2002) computed a water mass density census in a realistic ocean model, and inferred the spurious dianeutral transport based on census changes, while neglecting effects from the nonlinear equation of state. Getzlaff et al. (2010) assess available methods appropriate for idealized situations with a linear equation of state.

This paper re-examines and updates the conclusions of Griffies et al. (2000), expanding the analysis to cover more models, with more detailed analysis, and ultimately estimates the numerical mixing in the context of realistic global ocean models. To investigate the numerical mixing, we systematically perform a hierarchy of idealized experiments examining the solution behavior as a function of numerical parameters, primarily the grid Reynolds number ($Re_{\Delta x} = U_c \Delta x / \nu$). For each of the four different idealized problems, we examine solutions obtained with four different ocean models and try to understand what is the main mechanisms that control the spurious mixing. The diagnostic we use is the reference potential energy (RPE) proposed by Winters et al. (1995). The RPE is a single global number that reflects the effect of dianeutral transport in a closed system. Our main findings are that the grid Reynolds number is the dominant controlling parameter for diapycnal numerical mixing. Low $Re_{\Delta x}$, either due to high resolution or viscosity, leads to less grid-scale noise and thus to less spurious mixing.

Section 2 describes the numerical models used in this study and the potential energy method used to

diagnose spurious dianeutral transport. Sections 3, 4, 5 and 6 present results and analysis for the idealized test cases consisting of a lock-exchange, an overflow on a slope, an internal wave, and baroclinic eddies in a channel, respectively. Section 7 provides an assessment of the spurious mixing seen in the idealized tests. Section 8 presents results from realistic global simulations using GOLD and MOM, both in non-eddy and eddy configurations. We present our conclusions in Section 9.

2. Models, tests, and analysis methods

Here we summarize the model codes used in this study, introduce the test cases, and present the analysis methods used to diagnose spurious dianeutral transport.

2.1. Model codes and advection schemes

We investigate spurious dianeutral transport in the following four codes.

- **GOLD:** The Generalized Ocean Layer Dynamics provides a C-grid ocean code, used here in its isopycnal formulation (Adcroft et al., 2008; Hallberg and Adcroft, 2009; Ilıcak et al., 2011). GOLD provides us with a baseline for the minimum spurious diapycnal mixing realizable in both the idealized and realistic tests considered in this paper.
- **ROMS:** The Regional Ocean Modeling System is a C-grid ocean code, used here in its stretched terrain-following formulation (Shchepetkin and McWilliams, 2005).
- **MITGCM:** The MIT general circulation model (Marshall et al., 1997) is a C-grid ocean code, used here with the z^* level coordinate formulation of Stacey et al. (1995) and Adcroft and Campin (2004). Bottom topography is represented using the partial step method of Adcroft et al. (1997).
- **MOM:** The Modular Ocean Model (Griffies, 2009) is a B-grid ocean code, used here with the z^* level coordinate formulation as in MITGCM. Bottom topography is represented using the partial steps of Pacanowski and Gnanadesikan (1998), which is directly analogous to that used in the MITGCM.

All ocean codes used in this study employ the Boussinesq hydrostatic primitive equations,

although some codes have options for non-Boussinesq and/or non-hydrostatic approaches. In addition, convective adjustment and explicit diffusion parameterizations are removed in all models.

Griffies et al. (2000) evaluated five different tracer advection schemes under the premise that more sophisticated advection schemes reduce the spurious dianeutral transport. In the present study, we focus primarily on one tracer advection scheme for each model code, with each scheme flux limited to retain physically appropriate values, typically enforcing a monotonicity constraint. The advection schemes are chosen based on their proven utility within a number of applications with the respective model codes.

- GOLD: Piecewise linear method (PLM).
- ROMS: Multidimensional positive definite advection transport algorithm (MPDATA), which is a third order accurate scheme (Margolin and Smolarkiewicz, 1998).
- MITGCM: 7th-order monotonicity preserving advection scheme of Daru and Tenaud (2004).
- MOM: Multi-dimensional piecewise parabolic method (PPM), which is third order accurate scheme, implemented with a monotonicity constraint according to Colella and Woodward (1984); Lin (2004).

2.2. Suite of test cases

We examine the spurious dianeutral transport in a suite of tests that have direct relevance to the ocean climate problem. For this purpose, we consider four idealized tests and one realistic global test.

- LOCK-EXCHANGE OR DAM BREAK: A vertical density front separates two density classes. Adjustment occurs in which lighter water moves above heavier water.
- OVERFLOW: A vertical density front separates two density classes, with the heavier water initially sitting on a shallow shelf. Adjustment occurs in which the heavy water flows downslope, filling the abyss with dense water.
- INTERNAL WAVE: An internal gravity wave propagates in a vertically stratified flow, with both a small and a large amplitude considered.
- EDDYING CHANNEL: A baroclinically unstable channel model, in which a mesoscale eddy field develops.

- GLOBAL OCEAN: Our final test considers the spin-down of a global ocean climate model using both GOLD and MOM at non-eddying and eddy permitting grid resolutions.

These experiments progressively increase in complexity, but our analysis of the first experiment is most extensive since our conclusions generally carry forward. The idealized tests employ an equation of state that is linearly dependent on temperature, whereas the realistic global test employs the full nonlinear equation of state for seawater.

2.3. Diagnosing spurious dianeutral transport

In the analysis presented here, we focus on a single global number; namely, the *reference potential energy* (RPE) as used by Winters et al. (1995). The RPE is the minimum potential energy obtained by sorting the density without mixing; the RPE is the unavailable potential energy. The RPE changes only via dianeutral transport, with mixing generally increasing the RPE (Winters et al., 1995; Özgökmen et al., 2009; Ilıcak et al., 2009).

To compute the RPE, all water parcels in the global domain are sorted, with the heaviest parcels at the bottom and lighter parcels above. The sorting results in a redistribution of the parcels throughout the model domain and a sorted density state ρ^* . The reference potential energy is then calculated as the volume integral of the density-weighted geopotential:

$$RPE = g \iiint \rho^* z dV \quad (1)$$

Appendix A provides some added details for computing the RPE. RPE increases when density is mixed; that is, when work is applied to the ocean, either via spurious numerical sources or physical mixing processes. Hence, in an ocean domain closed to boundary fluxes of buoyancy, evolution of the RPE directly reflects a nonzero dianeutral transport. For the various test simulations, we examine the evolution of the non-dimensional reference potential energy

$$\overline{RPE}(t) = \frac{RPE(t) - RPE(t=0)}{RPE(t=0)}, \quad (2)$$

which shows the relative change of the RPE with respect to the initial state. The relative RPE removes uninteresting differences in RPE due to slight geometry differences between the different model codes.

The main limitation of the RPE based method is that it provides no information about where diapycnal transport occurs in the ocean domain. Geographical information must be obtained via complementary approaches, such as the diffusivity-based approaches of Griffies et al. (2000); the passive tracer approaches of Getzlaff et al. (2010), and Hill et al. (2011); or the “noise” diagnostic suggested by Jochum et al. (2008). We accept this limitation of the potential energy approach for the present study, since the method proves robust across the test suite and four model codes considered.

A further limitation of the RPE method, also shared by Griffies et al. (2000), is we are able to identify spurious diapycnal mixing only for the case of zero surface buoyancy flux. Hence, the diagnosis occurs in a system that is undergoing an adjustment that generally differs from more realistic cases with surface buoyancy fluxes. This limitation is fundamental to the methods that diagnose spurious diapycnal transport via a sorting approach.

Although we use an adiabatically sorted state to compute the RPE, we refrain from diagnosing a local, or isopycnally averaged, diffusivity from the sorted profile, for the two reasons given in the introduction; the diagnosed diffusivity is noisy and potentially misleading. Examining the potential energy of mixing, via the evolution of RPE, is both robust (not noisy), and relevant to global energetics of the ocean.

3. Lock-exchange

Here, we analyze the spurious diapycnal transport arising from a lock-exchange / dam break test case. The configuration includes no rotation and is two-dimensional.

3.1. Model configuration

The model configuration is similar to the non-rotating gravitational adjustment problem described in Haidvogel and Beckmann (1999). The computational domain is two-dimensional, with horizontal dimension $0 \leq x \leq L$ and vertical dimension $-H \leq z \leq 0$, where $L = 64$ km and $H = 20$ m. Insulated conditions are used for temperature and salinity on all boundaries. The C-grid models all use no-flow and free-slip bound-

ary conditions for velocity components, whereas the B-grid MOM simulation uses no-slip side boundaries and free slip on the bottom. The lock-exchange problem is initialized with dense (cold) fluid on the left separated from the light (warm) fluid on the right (see Figure 1 (a))

$$T(x, y, z) = 5^\circ\text{C} \quad \text{where} \quad 0 \leq x < L/2, \quad (3)$$

$$T(x, y, z) = 35^\circ\text{C} \quad \text{where} \quad L/2 \leq x \leq L. \quad (4)$$

Salinity remains a constant at 35 psu throughout the domain, with density a linear function of temperature. The initial density contrast ($\delta\rho$) across the vertical front is 5 kg m^{-3} .

The horizontal grid spacings are 500 m, 1 km, 2 km, and 4 km in all codes. Four different vertical resolutions are employed; $\Delta z = 10$ m (2-layer), $\Delta z = 5$ m (4-layer), $\Delta z = 2$ m (10-layer), and $\Delta z = 1$ m (20-layer). The vertical grid spacing is uniform in ROMS, MITGCM and MOM. Thus, all codes have the same nominally constant vertical resolution. In GOLD, we employ 21 isopycnal layers, however only two of them have finite amplitude, the other layers have angstrom thicknesses (10^{-10} m). Since MITGCM does not use time splitting, we decided to set the barotropic and baroclinic time steps equal to each other in all models. Baroclinic and barotropic time steps are set to 1 second for all grid spacings, for a maximum lateral CFL number of order 10^{-3} at the highest resolution.

For each simulation, the tracer concentration evolves solely through the numerical advection operator. In the base cases, the lateral Laplacian viscosity is $10^{-2} \text{ m}^2 \text{ s}^{-1}$, and the vertical viscosity is $10^{-4} \text{ m}^2 \text{ s}^{-1}$. We later explore simulations with larger lateral viscosities.

3.2. GOLD simulation

When the vertical wall is removed at time zero, the density layers adjust at the internal gravity wave speed to form a two-layer exchange flow. We integrate the simulations until the fronts reach boundaries. Figure 1b shows the temperature field in a two-layer GOLD simulation 17 hours into the adjustment. The initial vertical front has separated into left and right propagating fronts separated by a relatively flat interface. Note the absence of any mixing between the density classes, reflecting the absence of any spurious diapycnal mixing. At these resolutions with finite viscosity, the flow re-

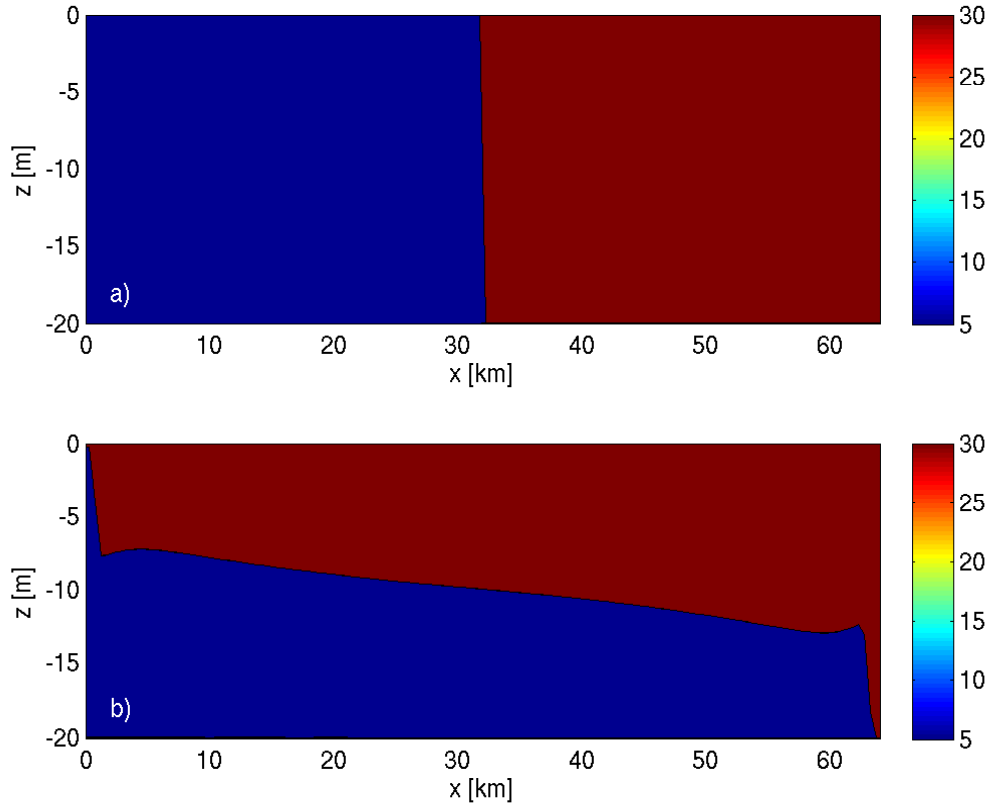


Fig. 1. (a) Top panel: Initial temperature for the lock-exchange test case, consisting of two discrete temperatures. (b) Lower panel: Temperature for the GOLD simulation after 17 hours of simulation. This configuration used a horizontal grid spacing of $\Delta x = 500$ m, a lateral Laplacian viscosity is $10^{-2} \text{ m}^2 \text{ s}^{-1}$, vertical viscosity of $10^{-4} \text{ m}^2 \text{ s}^{-1}$, and zero explicit tracer mixing. Note the absence of any exchange of fluid between the two density classes, indicative of a simulation with identically zero spurious diapycnal transport.

mains laminar. This simulation is used as a benchmark for all others in this section.

3.3. Sensitivity to grid spacing in MITGCM, MOM, and ROMS

Now, we explore the sensitivity of the dam break simulation to both vertical and horizontal grid spacing in MITGCM, MOM, and ROMS. As expected, the finer the grid resolution, the better the simulations agree with the GOLD case. Furthermore, these test cases reveal some fundamental differences between the simulations with ROMS versus those in MITGCM and MOM; an upstream-biased momentum advection scheme used in ROMS leads to less spurious mixing.

3.3.1. Sensitivity to vertical grid spacing

Figure 2 shows the temperature at the same time for the non-isopycnal simulations with a horizontal grid spacing of $\Delta x = 500$ m and with various vertical grid spacings. In contrast to the GOLD simulation, note that new density classes are spuriously formed as the front widens.

The top panel in each column of Figure 2, when compared to the lower panels of the same column, show how the gravity currents propagate more slowly with the coarser vertical grid spacing. The distance propagated by the front is reduced when the density anomaly is diluted by spurious mixing. Spurious mixing is largest when there are only two vertical levels in MITGCM, MOM, and ROMS ($\Delta z = 10$ m). Such large spurious mixing is inevitable with only two vertical levels, since with only two grid points, the numerical advection operator re-

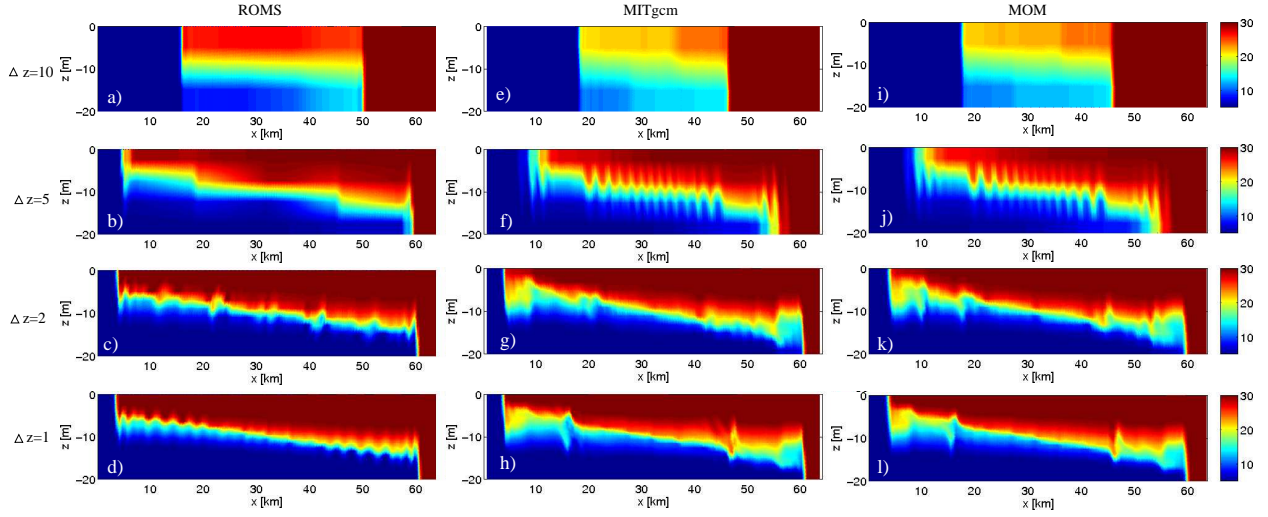


Fig. 2. Temperature at time=17 hours for the dam break test cast run with a horizontal grid spacing of $\Delta x = 500$ m. Vertical grid spacing is refined moving from top to bottom: (a), (e), (i) $\Delta z = 10$ m ; (b), (f), (j) $\Delta z = 5$ m ; (c), (g), (k) $\Delta z = 2$ m ; (d), (h), (l) $\Delta z = 1$ m.

duces locally to first order upwind in the vertical. When the vertical spacing is refined to $\Delta z = 5$ m, the spurious mixing is reduced, though note the presence of extraneous undulations in MITGCM and MOM [Figures 2 (f) and (j)], whereas the ROMS simulation is smoother [Figure 2 (b)].

The density front is more sharply defined when the vertical grid spacing is further refined to $\Delta z = 2$ m. MITGCM and MOM have similar temperature fields including a “head” of gravity current at $x = 58$ km in Figures 2 (g) and (k). Significant mixing occurs at the head due to high vertical velocities. The ROMS simulation starts to look like GOLD at this grid spacing, with noticeably less noise at the head and the tail [Figure 2 (c)] than at coarser resolution. In the finest vertical grid spacing ($\Delta z = 1$ m), the noise in both MITGCM and MOM is reduced, and the ROMS simulation has a narrower interfacial layer between dense and light layers [Figure 2 (d)].

Benjamin (1968) derived a theory for the steady propagation of a gravity current in a rectangular channel. Using Bernoulli’s equation for an ideal fluid, he derived the flow speed as

$$u_f = \frac{1}{2} \sqrt{gH(\delta\rho/\rho_0)}. \quad (5)$$

Figure 3 shows the front locations as a function of time for a) $\Delta z = 10$ m and b) $\Delta z = 1$ m. The coarse vertical spacing exhibits flow that is slower than the theoretical values, with the slowdown arising from the spurious mixing between layers (Figure 3(a)). We note that the front speed in ROMS

is closer to the analytical speed than MITGCM and MOM, even though with only two grid points in the vertical they all use first order upwind advection in the vertical. With refined vertical grid spacing, all front velocities approach the analytical value [Figure 3(b)].

Figure 4(a) displays the time evolution of the RPE normalized by the initial RPE for different models with different vertical grid spacings, holding the horizontal grid at $\Delta x = 500$ m. The GOLD simulation with no explicit diapycnal diffusivity retains a constant RPE to machine precision (cyan line in Figure 4(a)). As explained later in Section 3.6, the RPE of all the other models is broadly parabolic in time; an increasing rate of change indicates increasing volume-integrated work done by spurious numerical mixing.

The MITGCM and MOM simulations yield similar RPE curves for each vertical grid spacing, so much so that the coarsest resolution curves overlay each other almost exactly (blue dotted and dashed lines). For any particular vertical grid spacing, the ROMS RPE (solid) is lower than either of the corresponding MITGCM (dashed) or MOM curves (dotted). This result is consistent with the front speed analysis, in which ROMS showed closer agreement to theory and GOLD than either MITGCM or MOM. Refining vertical grid spacing for MITGCM, MOM, and ROMS reduces the numerical mixing.

Although all models have different tracer advection schemes (ranging from third to seventh order), the similarity in implied mixing between the

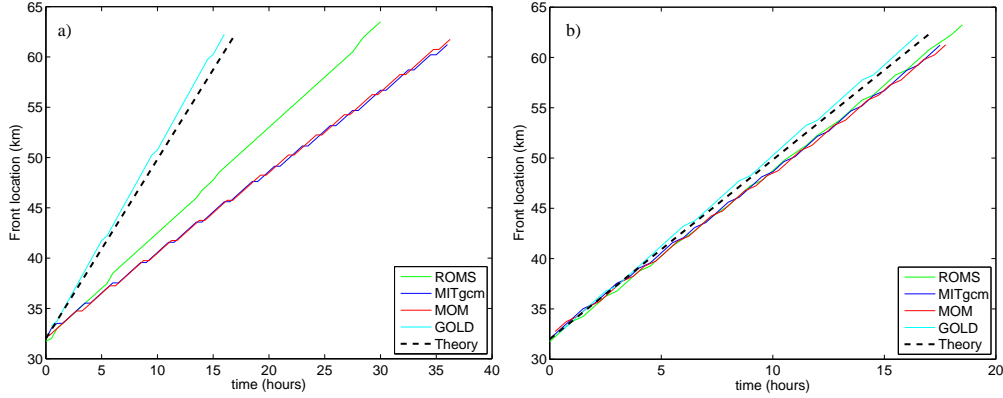


Fig. 3. Front locations in the dam break simulation for different model codes when (a) $\Delta z = 10$ m and (b) $\Delta z = 1$ m.

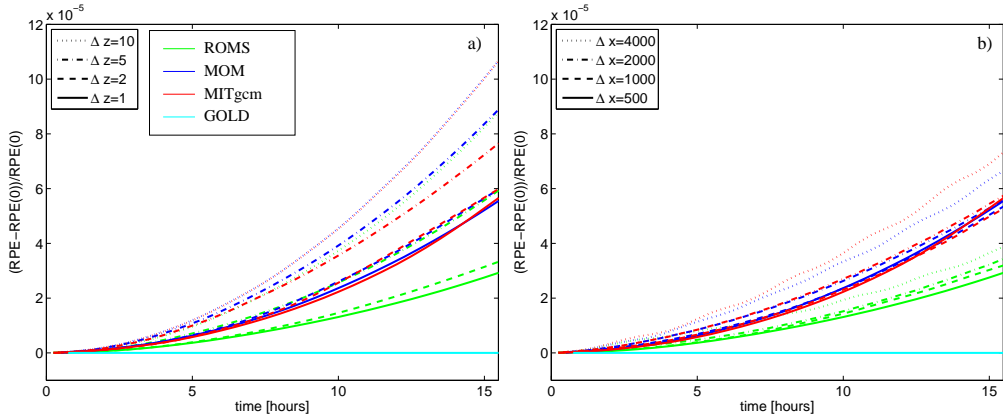


Fig. 4. Time evolution of the normalized reference potential energy \overline{RPE} . (a) Different models all using a horizontal grid spacing of $\Delta x = 500$ m and with various vertical grid spacings. (b) Different models all using a vertical grid spacing of $\Delta z = 1$ m with different horizontal grid spacings.

MITGCM and MOM suggests the order of accuracy has little impact for this test case at the grid spacings chosen. This result suggests that the numerical mixing is dominated by the flux limiters used to eliminate tracer extrema, with such flux limiting in effect reducing the advection scheme to first order upwind. However, this behavior does not explain why ROMS has less mixing than MITGCM or MOM, since the tracer advection scheme in ROMS is not fundamentally different than MITGCM or MOM.

3.3.2. Sensitivity to horizontal grid spacing

Figure 4(b) shows the influence on spurious mixing of varying horizontal grid spacing from $\Delta x = 4000$ m to $\Delta x = 500$ m, while keeping the vertical grid spacing at $\Delta z = 1$ m. The results are broadly similar to those when varying the vertical grid spacing, with a refined horizontal spacing decreasing the numerical mixing; and MITGCM and MOM

always having more mixing than ROMS.

3.4. Sensitivity to momentum transport and lateral viscosity

The consistent differences between ROMS on the one hand, and MITGCM and MOM on the other, are quite striking. These results reveal a key element in the spurious mixing question related to the treatment of momentum transport and momentum closure.

Both MITGCM and MOM use second order centered operators for momentum transport, with an associated specification of a friction operator to dissipate noise arising from dispersion errors. The friction operator is tunable, with small viscosities allowing for relatively high grid Reynolds number Re_{Δ} . However, since the transport operator is unbiased and linear, the high Reynolds number comes

at the price of enhanced grid scale energy that can manifest as noise. This feature of noisy high grid Reynolds number flow can be seen from an analysis of the steady state discrete advection-diffusion equation using second order numerics (e.g., Bryan et al., 1975; Griffies, 2004). That analysis indicates that dissipation of spurious grid scale noise requires that the grid Reynolds number, defined as

$$\text{Re}_\Delta = \frac{U\Delta}{\nu_h}, \quad (6)$$

should be less than 2. Here Δ is the horizontal grid spacing, ν_h the specified lateral viscosity, and U is the characteristic velocity scale.

In contrast to MITGCM and MOM, ROMS uses a third-order, upstream-biased, dissipative advection scheme for momentum, implemented with a predictor-corrector time-step algorithm (Shchepetkin and McWilliams, 2005; Marchesiello et al., 2009). This momentum advection operator allows for the retention of steep gradients without incurring as much noise as for a second order scheme, thus enhancing the effective resolution for a given grid size (Shchepetkin and McWilliams, 1998). As above, the stability condition preventing spurious numerical modes and unphysical extrema requires $\text{Re}_\Delta < 2$ (Marchesiello et al., 2009; Anderson et al., 1984). This stability criteria is enforced through the introduction of local dissipation, implemented as part of the momentum advection scheme. That is, numerical dissipation is wrapped into the momentum advection operator. Consequently, the use of explicit viscosity through either a Laplacian or bi-harmonic operator is rendered unnecessary for numerical purposes.

Recognition that grid-scale noise in the velocity fields enhances numerical mixing of transported scalars (Griffies et al., 2000) is consistent with the above performance of ROMS. Namely, the adaptive dissipation of momentum minimizes the grid-scale velocity variance. This result is of fundamental importance when considering spurious diapycnal transport.

To test this result with MITGCM and MOM requires the use of an explicit viscous dissipation operator. We therefore reconsider the dam break test with a suite of lateral viscosities, thus examining the sensitivity of spurious diapycnal mixing to the lateral grid Reynolds number. We compute the grid Reynolds number as

$$\text{Re}_\Delta \approx u_f \Delta / \nu_h, \quad (7)$$

where u_f is the theoretical gravity current wave speed (Equation (5)), which is approximately 0.5 m/s using the initial density difference.

Figure 5 shows the temperature fields of the MITGCM and MOM simulations using a suite of lateral viscosities, with fixed horizontal and vertical grid spacings of $\Delta x = 500$ m and $\Delta z = 1$ m. The lateral viscosity is varied across the values 0.1, 1, 10, 100, 200 m^2/s , corresponding to grid Reynolds numbers, respectively, of 2500, 250, 25, 2.5 and 1.25. As expected, increasing the lateral viscosity, or reducing the grid Reynolds number, decreases the spurious mixing in both MITGCM and MOM. Doing so also suppresses the vertical undulations (behind the fronts), thus making the lower grid Reynolds number case more like a two-layer dam break flow found in GOLD [Figures 5(e) and (j)].

The interface between the density layers becomes sharper as the grid Reynolds number decreases, indicating that the numerical mixing reduces as grid Reynolds number reduces. However, the interface between the upper and lower layers is also tilted compared to the GOLD simulation [Figure 1(b)]. High lateral viscosity also smooths the vertical shear (not shown). This result indicates that the physical processes are modified, perhaps detrimentally, with too high viscosity.

The time rate of RPE change at time $t = 17$ hours is shown in Figure 6 as a function of Re_Δ . The spurious numerical mixing is high and steady (capped) when the grid Reynolds number is larger than 100. Changing horizontal grid spacing or viscosity does not reduce the spurious mixing in this regime, presumably because the grid noise amplitude is too high in the velocity field, thus making the tracer advection schemes default to their first order upwind limiters locally. However, when Re_Δ is below 100, the numerical mixing decreases rapidly with decreasing Re_Δ . In particular, the spurious mixing at $\text{Re}_{\Delta x} < 5$ is an order of magnitude smaller than that at $\text{Re}_{\Delta x} > 100$.

3.5. A cautionary remark on non-monotonic advection schemes

We offer here a cautionary remark on the use of advection schemes without flux limiters. For this purpose, consider the second order moment (SOM) tracer advection scheme of Prather (1986). This scheme has been found in certain studies to

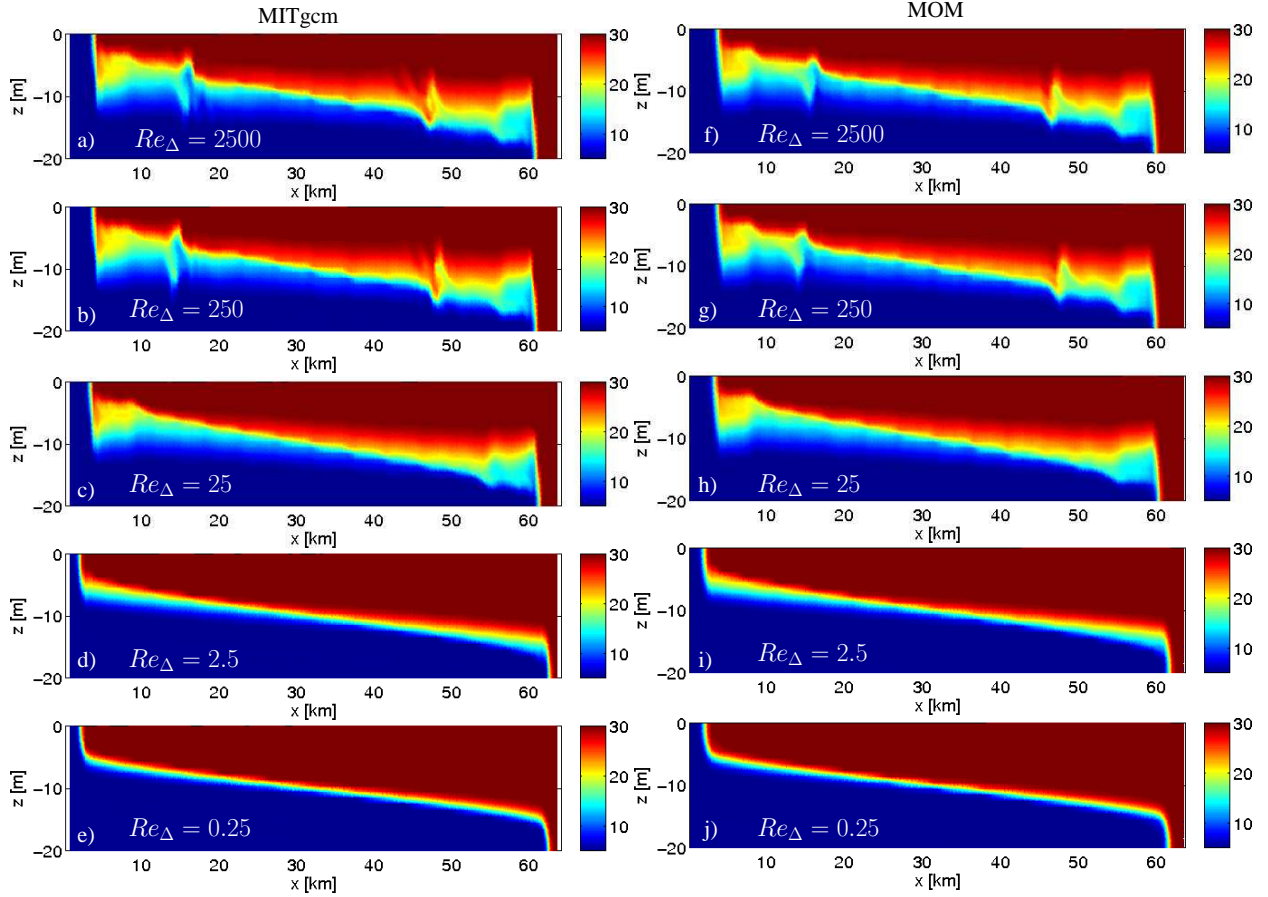


Fig. 5. Temperature at time=17 hours for the dam break test case for MITGCM and MOM, when run with a suite of lateral viscosities, with viscosity increasing as we move down in the figure. The horizontal and vertical grid spacings are $\Delta x = 500$ m and $\Delta z = 1$ m, relatively. The left column shows MITGCM and right column shows MOM. (a) and (f) $\nu_h = 0.1$ m²/s and $Re_\Delta = 2500$, (b) and (g) $\nu_h = 1$ m²/s and $Re_\Delta = 250$, (c) and (h) $\nu_h = 10$ m²/s and $Re_\Delta = 25$, (d) and (i) $\nu_h = 100$ m²/s and $Re_\Delta = 2.5$, (e) and (j) $\nu_h = 200$ m²/s and $Re_\Delta = 2.5$.

be quite useful at retaining strong tracer gradients, and is thus used for many applications in sea ice and ocean modelling (e.g., Merryfield and Holloway, 2003; Maqueda and Holloway, 2006; Tatebe and Hasumi, 2010; Hill et al., 2011). The results with Prather tracer advection are compared to the monotonic 7th-order scheme, both implemented in the MITGCM (Daru and Tenaud, 2004). We also performed the same test with the MOM implementation of Prather advection, with the results similar to those in the MITGCM (not shown). Notably, we do not apply a flux limiter to the SOM scheme, in order to retain the full accuracy of the scheme, and to reflect common usage in the literature. However, as detailed below, we find the use of a flux limiter to be essential, even for the Prather scheme.

Figure 7 displays the probability density functions (pdf) of the density field for the lock-

exchange case. Initially, there are two water masses ($\rho_{min} = 1022$ kg m⁻³ and $\rho_{max} = 1027$ kg m⁻³) and each contains 50% of the total volume (Figure 7(a)). The pdf of the flux limited 7th-order scheme is shown at time=17 hours in Figure 7(b). Absent spurious mixing or dispersion, the pdf will remain unchanged. However, the percentile of the minimum and maximum density decreases considerably, as new water is formed by numerical mixing with densities between the ρ_{min} and ρ_{max} .

Figure 7(c) shows the pdf using the Prather scheme after 17 hours. Note the new water masses with densities outside of the initial range. The percentile values for these new water masses are significantly higher than for any intermediate densities. These new extrema arise in this test because the Prather SOM scheme is unlimited while the 7th-order scheme is limited.

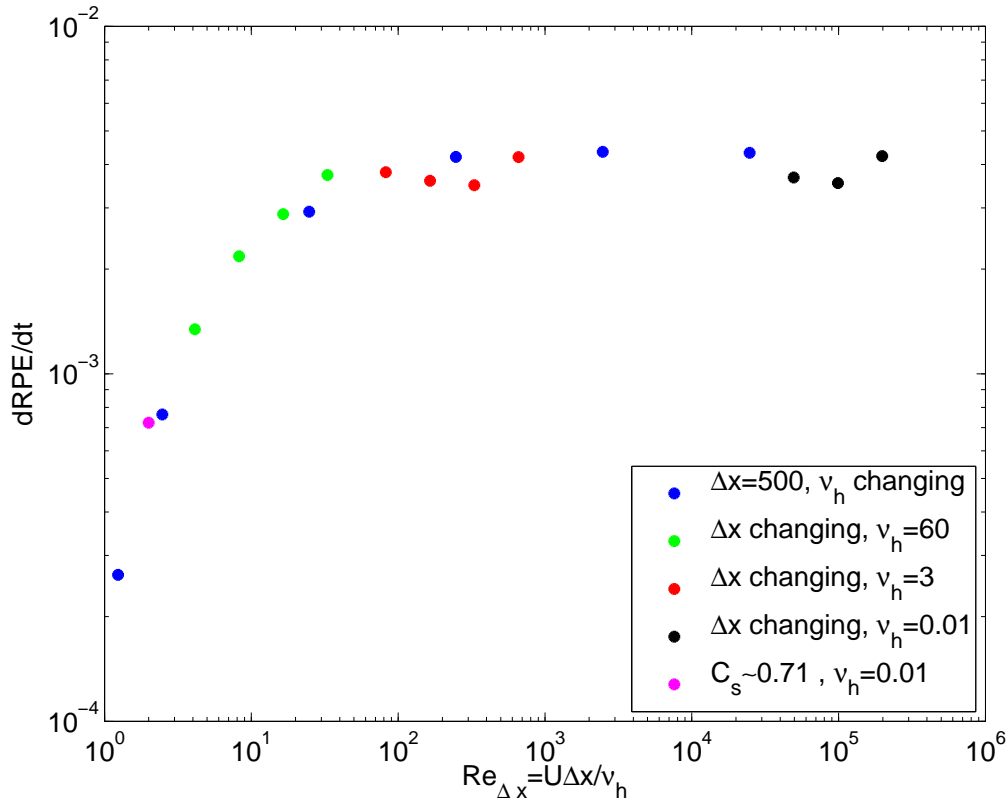


Fig. 6. Rate of change of the reference potential energy [Watts m^{-2}] in the MITGCM at simulation time 17 hours as a function of lateral grid Reynolds number, $Re_{\Delta x} = U\Delta x/v_h$, using vertical grid spacing of $\Delta z = 1$ m. There are five different sets of simulations exhibited in this figure: (i) $\Delta x = 500$ m with v_h changing (blue dots), (ii) Δx changing with $v_h = 60$ m^2/s (green dots), (iii) Δx changing with $v_h = 3$ m^2/s (red dots), (iv) Δx changing with $v_h = 0.01$ m^2/s (black dots) (v) Smagorinsky viscosity with $\Delta x = 500$ m and $v_h = 0.01$ m^2/s (magenta dot).

The normalized reference potential energy is shown in Figure 7(d). Notably, the Prather scheme appears to have less spurious numerical mixing compared to the 7th-order scheme. The reason is that the false extrema realized with the unlimited Prather scheme are decreasing the RPE. Hence, an inferred numerical mixing *appears* low in this non-monotonic scheme since the extrema are not conserved.

Note, however, there is comparable volume of new water in the middle of the pdf, implying comparable mixing in both 7th order and Prather schemes. We also note that the widely used positive definite limiter of Prather (1986) has no impact on these middle densities, as this limiter only has an affect in the vicinity of zero values that did not appear in this test. An attempt to use the monotonic limiter of Merryfield and Holloway (2003) failed to properly limit the fields (not shown), in either MITGCM or MOM. Reasons for this failure

are unknown.

We conclude that the unlimited Prather scheme may *appear* to have less mixing from an integrated energetic point of view, but that result arises through a spurious anti-diffusive effect associated with new extrema; this anti-diffusion partially compensates for the RPE increase from the generation of mixed water masses. Our experience indicates that such extrema, though arguably modest with the Prather SOM scheme in certain tests, are generally unacceptable in realistic modelling. We present this result not so much as a thorough examination of the Prather SOM scheme, but rather as a cautionary remark on the need to provide an accurate and robust flux limiter, even when the underlying tracer advection scheme is potentially very accurate.

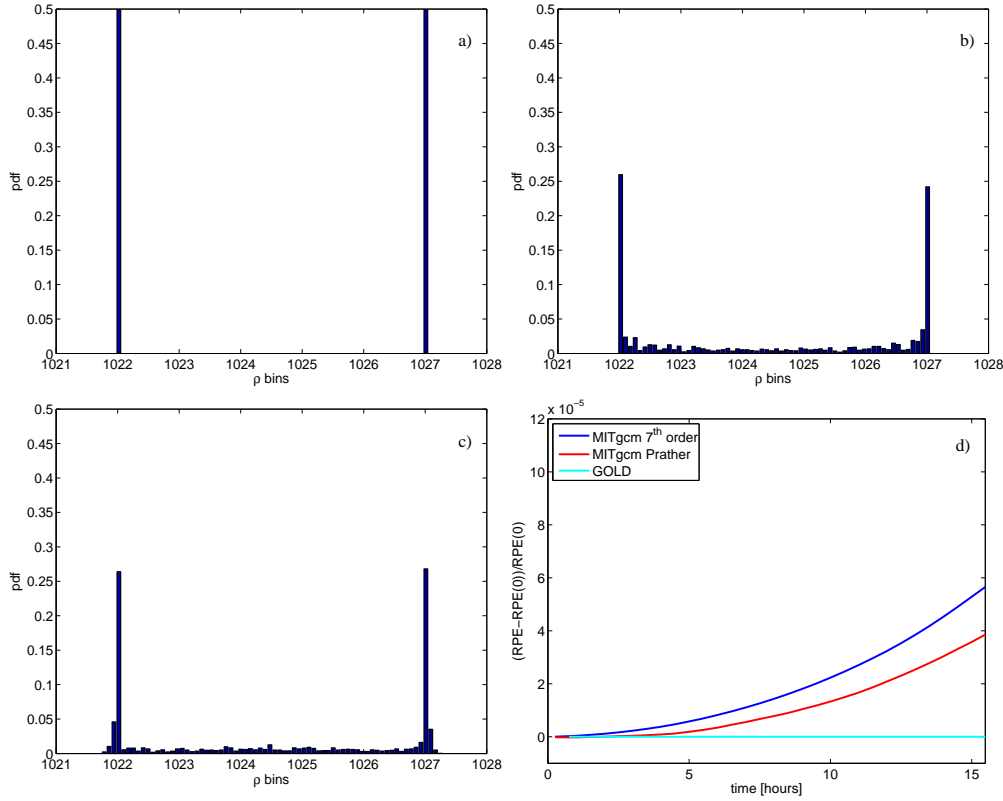


Fig. 7. (a) Initial condition of the probability density function of the temperature for the dam break test case. (b) The probability density function of the temperature for the monotonic 7th-order advection scheme after 17 hours of simulation time. (c) The probability density function of temperature for the Prather advection scheme after 17 hours. (d) Time evolution of the normalized reference potential energy \overline{RPE} for the different advection schemes. Each of these simulations uses a horizontal grid spacing of $\Delta x = 500$ m, vertical grid spacing of 1 m, vertical viscosity of 10^{-4} m² s⁻¹, and lateral viscosity of 10^{-2} m² s⁻¹.

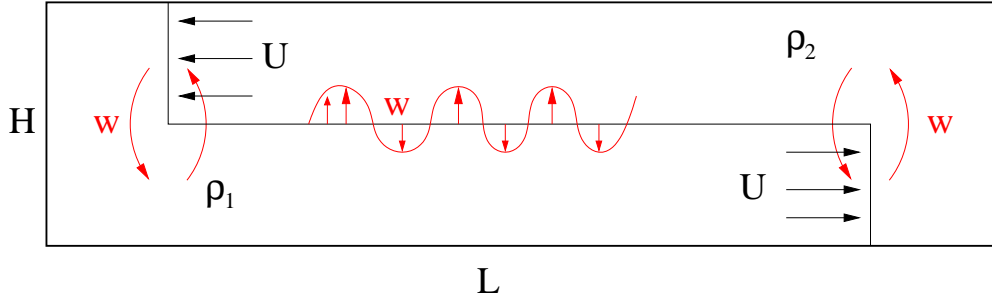


Fig. 8. Schematic diagram of mixing (predominantly in the red regions) during gravitational adjustment in the dam break test case. See main text for detailed discussion of this figure.

3.6. A conceptual picture of spurious mixing in the dam break test

The results for spurious diapycnal mixing in the lock-exchange / dam break test case suggest the following conceptual picture. After release of the vertical wall between the two fluids, a two-layer system forms, with fronts travelling at the internal

gravity phase speed (see Equation (5)) in opposite directions. A schematic diagram of this adjustment is shown in Figure 8.

There are two primary regions of spurious diapycnal mixing. The first is the lateral interface behind the two fronts. This area increases linearly in time as the fronts move away from each other. For the simulations with nontrivial spurious dia-

neutral mixing, there are strong vertical velocities occurring at small scales in this region [small red arrows in Figure 8]. Since the distance between the two fronts is increasing $O(t)$, the contribution to RPE change by spurious mixing in this area scales as $O(t^2)$.

The second region of the spurious numerical mixing is the near vertical head of the gravity current. The light/heavy water in front of the gravity current head has to displace up/down such that lateral flow is strongly divergent. This contribution to RPE is approximately constant in time because the height of fluid in the head is essentially unchanging.

High spatial variability in the vertical velocities between the fronts is therefore the dominant cause of spurious diapycnal mixing in this test case. That is, the noisy vertical velocity prompts the advection schemes to introduce a nontrivial degree of flux limiting, which renders large spurious diapycnal mixing. These vertical velocities correspond to noisy divergences in the horizontal velocity field, related to large energy in the velocity field at or near the horizontal grid scale. Increases in lateral viscosity are effective at reducing the horizontal grid Reynolds number, Re_Δ . Reducing Re_Δ to values no larger than roughly 10 – 50 has been found effective at reducing the noisy horizontal divergences, reducing grid noise in the vertical velocity, and thus squelching the spurious mixing. Notably, the ROMS simulation, with viscous dissipation built into its momentum transport, ensures the flow field is smooth at the grid scale. In turn, ROMS consistently shows the best results for this test case amongst the non-isopycnal simulations.

4. Overflow test case

To investigate the impact of topography on spurious mixing, we consider a non-rotating overflow configuration similar to that described in Haidvogel and Beckmann (1999). The domain is a 2000 m deep, two-dimensional (x - z) steep topographic slope initialized with dense water on the shelf. The velocity field is initially at rest. A vertical density front with a 2 kg m^{-3} difference is located at $x = 20 \text{ km}$. There is initially no stratification in the off-shelf region. The geometry and initial conditions are illustrated in Figure 9(a). This test case is directly analogous to the dam break of Section 3, only now with a topographic slope down which

the dense water flows.

We hold the horizontal grid spacing constant at $\Delta x = 1 \text{ km}$ while considering three different vertical grid spacings:

- (i) $\Delta z = 40 \text{ m}$ (50-layers)
- (ii) $\Delta z = 30.3 \text{ m}$ (66-layers)
- (iii) $\Delta z = 20 \text{ m}$ (100-layers).

The vertical viscosity is held constant throughout the test suite at a value of $10^{-4} \text{ m}^2/\text{s}$. Lateral viscosity is varied from a small value of $\nu_h = 10^{-2} \text{ m}^2/\text{s}$, and increased to $10^3 \text{ m}^2/\text{s}$. We show results only from the finest vertical grid spacing; however, the coarse grid spacing results are qualitatively similar. Note that since ROMS uses a terrain following vertical coordinate, its effective vertical resolution is different than the z^* based MITGCM and MOM simulations in regions of shallow topography. Baroclinic and barotropic time steps are set to 10 seconds and 1 second, respectively.

Figures 9(b) and 9(c) show two snapshots from the GOLD simulation. After three hours, gravitational adjustment has accelerated the dense water towards the shelf-edge [Figure 9(b)], whereas after six hours, the gravity current has moved downslope and reached the bottom [Figure 9(c)]. The flow piles up at the front and a hydraulic jump occurs due to the sudden deceleration when the fluid reaches the bottom. Since there is no explicit diapycnal diffusivity prescribed for this simulation, density remains unmixed between the two initial water masses.

The ROMS simulations [Figures 9(d) and 9(e)] are qualitatively similar to GOLD. However, there is some production of intermediate waters during the initial gravitational adjustment, and significant entrainment by the time the gravity current reaches the bottom.

Simulations from both the MITGCM [Figures 9(f) and 9(g)] and MOM [Figures 9(h) and 9(i)] exhibit strong mixing for the same lateral viscosity ($\nu_h = 10^{-2} \text{ m}^2/\text{s}$) used in GOLD. The velocity fields are very noisy with this low viscosity, resulting in a near complete dilution of the dense water before the gravity current reaches the bottom in MITGCM and MOM [Figure 9(g) and 9(i)]. These results are reminiscent of those discussed by Winton et al. (1998) and Legg et al. (2006), who also used a relatively small lateral viscosity and thus a large grid Reynolds number. Increasing the viscosity to $1000 \text{ m}^2/\text{s}$ in both MITGCM and MOM causes the simulated flow to become more laminar, thus reducing spurious dilution of the dense water [Fig-

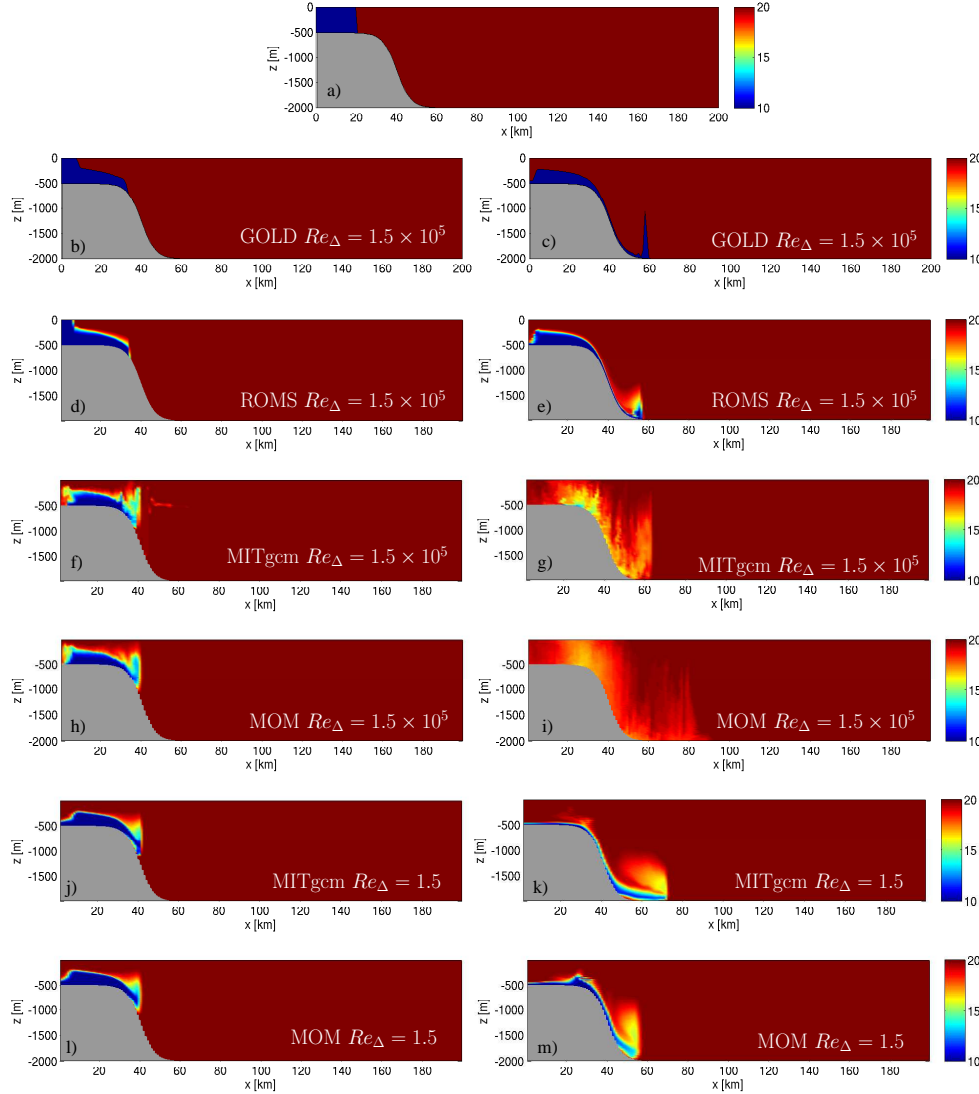


Fig. 9. Snapshots from the overflow test case, with each simulation using zero explicit diapycnal tracer diffusivity and $10^{-4} \text{ m}^2 \text{ s}^{-1}$ vertical viscosity. Top middle panel (a): Initial temperature, with cold dense water on the shallow slope, and light warm water throughout the remainder of the domain. The subsequent left column shows the simulations three hours after the initial condition, and the right column shows snapshots six hours afterward. Second row (b) and (c): simulations from GOLD with a lateral viscosity $\nu_h = 10^{-2} \text{ m}^2 \text{ s}^{-1}$. Third row (d) and (e): simulations from ROMS with a lateral viscosity of $\nu_h = 10^{-2} \text{ m}^2 \text{ s}^{-1}$. Fourth row (f) and (g): simulations with the MITGCM using a lateral viscosity of $\nu_h = 10^{-2} \text{ m}^2 \text{ s}^{-1}$. Fifth row (h) and (i): simulations with MOM using a lateral viscosity of $\nu_h = 10^{-2} \text{ m}^2 \text{ s}^{-1}$. Sixth row (j) and (k): simulations with the MITGCM using a lateral viscosity of $\nu_h = 10^3 \text{ m}^2 \text{ s}^{-1}$. Seventh row (l) and (m): simulations with MOM using a lateral viscosity of $\nu_h = 10^3 \text{ m}^2 \text{ s}^{-1}$.

ures 9(k) and 9(m)].

Figure 10 shows the rate of change of RPE as a function of grid Reynolds number. We used the characteristic velocity of the gravity current

$$u_f = 0.5 \sqrt{g(\delta\rho/\rho_0)H_o} \quad (8)$$

to compute the grid Reynolds number, with H_o the depth of the overflow water on the shelf (compare

to Equation (5) used for the dam break). The structure of the curves in Figure 10 are essentially the same for both the MITGCM and MOM simulations, and resembles the structure found for the dam break experiment (Figure 6). In particular, there is a plateau for the high grid Reynolds numbers, and an indication of scaling with Reynolds numbers below ~ 100 .

We conclude that to reduce spurious diapycnal mixing in the dam-break experiment, the grid Reynolds number should be small enough to suppress the grid noise and resolve the flow. This result is consistent with the conclusions of Legg et al. (2008), who argued that the bottom frictional boundary layers should be resolved to avoid spurious entrainment in the overflows.

5. Internal waves test case

We now examine spurious diapycnal mixing associated with the adjustment of an internal gravity wave in a stratified fluid without rotation or topography. The domain is a 500 m deep, 250 km wide, flat-bottomed rectangular basin. Two different initial states are used: a low amplitude isopycnal deformation in the middle of the domain [Figure 11(a)] and a high amplitude deformation [Figure 11(b)]. A linear equation of state is used and density depends only on temperature. The flow is linearly stratified by temperature with a constant buoyancy frequency of $N = 6.26 \times 10^{-3} \text{ s}^{-1}$. The horizontal and vertical grid spacings are 5 km and 25 m, respectively, for the MITGCM, MOM, and ROMS simulations, whereas GOLD uses the same horizontal grid spacing with 20 evenly spaced density layers. We integrate the simulations for 200 days without any bottom drag and with zero explicit diapycnal mixing. Baroclinic and barotropic time steps are set to 300 seconds and 10 seconds, respectively.

Figure 12 shows the temperature at 200 days for the GOLD, ROMS, MITGCM and MOM simulations employing small lateral viscosity, $\nu_h = 10^{-2} \text{ m}^2/\text{s}$. The initial amplitude was very small, and there is no visible erosion of the interface heights for any of the simulations. Time evolution of the reference potential energy is shown in Figure 12(e). There is no net increase of RPE in GOLD, due to the use of zero diapycnal diffusivity (cyan line). The other three codes exhibit very similar results for the first 50 days. Afterward, increase in RPE is lower in MOM than the ROMS and MITGCM simulations.

In contrast to previous experiments, the ROMS simulations are comparable to MITGCM and MOM. We conjecture that this behavior follows from the predominantly linear motion in this test, with the temperature equation mostly governed by vertical advection of the ambient stratification. The flow is therefore well-resolved. Hence, there is little

grid noise and nonlinear momentum advection is unimportant, so that the higher order ROMS numerical momentum advection scheme plays a negligible role.

The high amplitude internal wave results are shown in Figure 13. In this case, a reduction in temperature gradient in MITGCM, MOM, and ROMS is evident compared to the GOLD simulation [Figures 13(a), 13(b), 13(c) and 13(d)] near top and bottom, but with some increase in gradient in between. The time evolution of the RPE [Figure 13(e)] shows that the ROMS simulation has less spurious mixing in the high amplitude test case than MITGCM and MOM. Note that the RPE change in the high amplitude case is an order of magnitude larger than the RPE change in the low amplitude case. Although MOM has lower spurious mixing in the low amplitude case, it has higher mixing in the high amplitude [red line in Figure 13(e)]. These results are generally consistent with those described in Leclair and Madec (2011), who also found that increasing the amplitude of the internal waves increases the numerical mixing.

The rate of RPE change as a function of grid Reynolds number for the high amplitude test case is shown in Figure 14 for three simulations with lateral viscosities of $\nu_h = 1 \text{ m}^2/\text{s}$, $\nu_h = 15 \text{ m}^2/\text{s}$ and $\nu_h = 150 \text{ m}^2/\text{s}$, using both MITGCM and MOM. The characteristic velocity is computed as

$$U_c = \sqrt{2KE} \quad (9)$$

where $KE = (1/2) \mathbf{u}^2$ is the horizontal kinetic energy per mass, with \mathbf{u} the horizontal velocity. In all experiments, MITGCM simulations have lower spurious diapycnal mixing than MOM. This relative behavior may be due to the use of a 7th order tracer advection scheme in MITGCM, whereas MOM uses a third order scheme (Section 2.1). The numerical mixing is saturated at high grid Reynolds number and mixing starts to decrease when $Re_\Delta < 100$. The shape of the curve is similar to the previous test cases shown in Figure 6 and Figure 10.

6. Baroclinic eddies test case

We now introduce rotation and three spatial dimensions in the context of a simulation of baroclinic eddies. The domain consists of a horizontally periodic channel of latitudinal extent 500 km and longitudinal extent 160 km, with a flat bottom of 1000 m depth. The channel is on an f -plane with

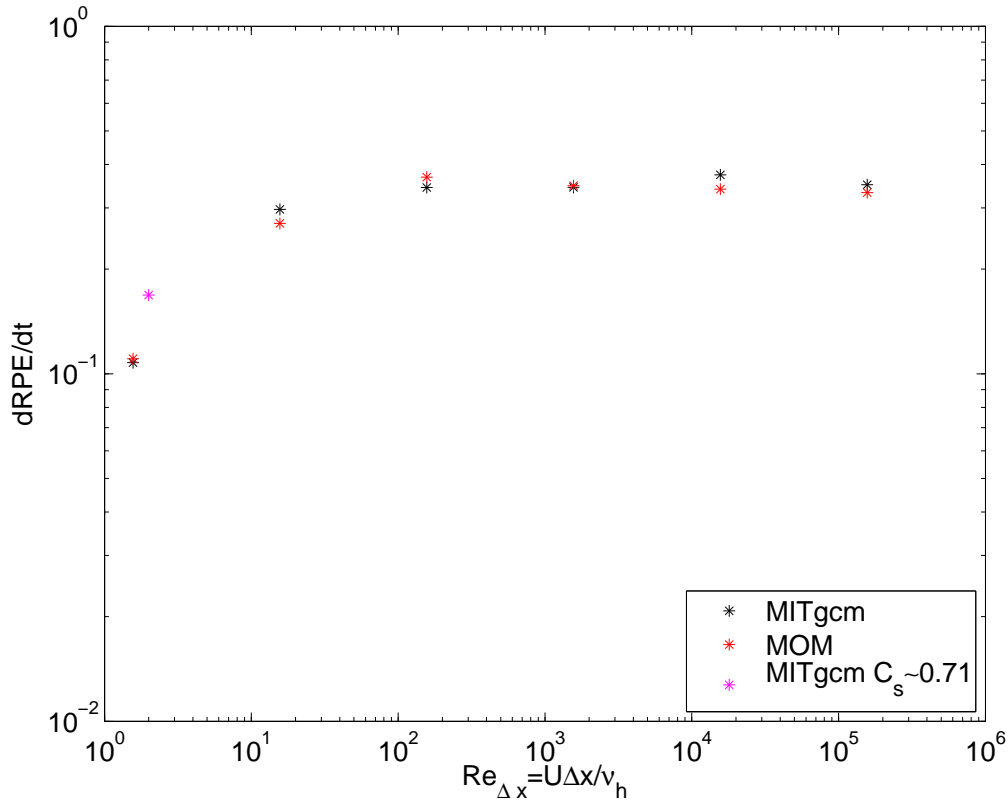


Fig. 10. Rate of change of the reference potential energy [Watts m^{-2}] in the overflow test case for the MITGCM and MOM, shown here as a function of grid Reynolds number.

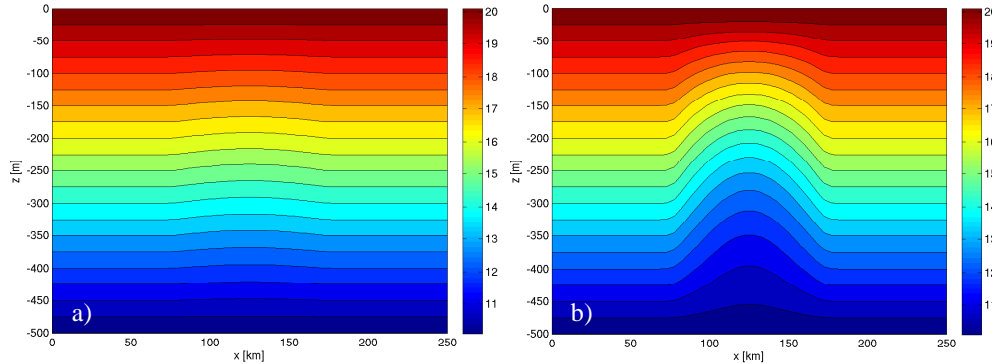


Fig. 11. Initial temperature for the internal wave tests. Panel (a) is the low amplitude test, and panel (b) is the high amplitude. The contour intervals are set according to the 20 layers used in the GOLD simulation.

the Coriolis parameter $f = 1.2 \times 10^{-4} \text{ s}^{-1}$ (roughly 55° latitude). The initial temperature profile is uniformly decreasing in the vertical with a horizontal gradient at the channel center (see Figure 15). The interface on the horizontal between north and south of the channel is a cosine shape with a wavelength of $x = 120 \text{ km}$. A quadratic bottom drag is used with dimensionless drag coefficient of $C_d =$

0.01. The large bottom drag coefficient and asymmetric initial condition promote baroclinic instability in the channel.

The first baroclinic Rossby radius of deformation is 20 km. We consider three different horizontal grid spacings, Δ , with the grid spacing the same in the two horizontal directions, $\Delta = \Delta x = \Delta y$. The finest grid spacing is $\Delta = 1 \text{ km}$, which re-

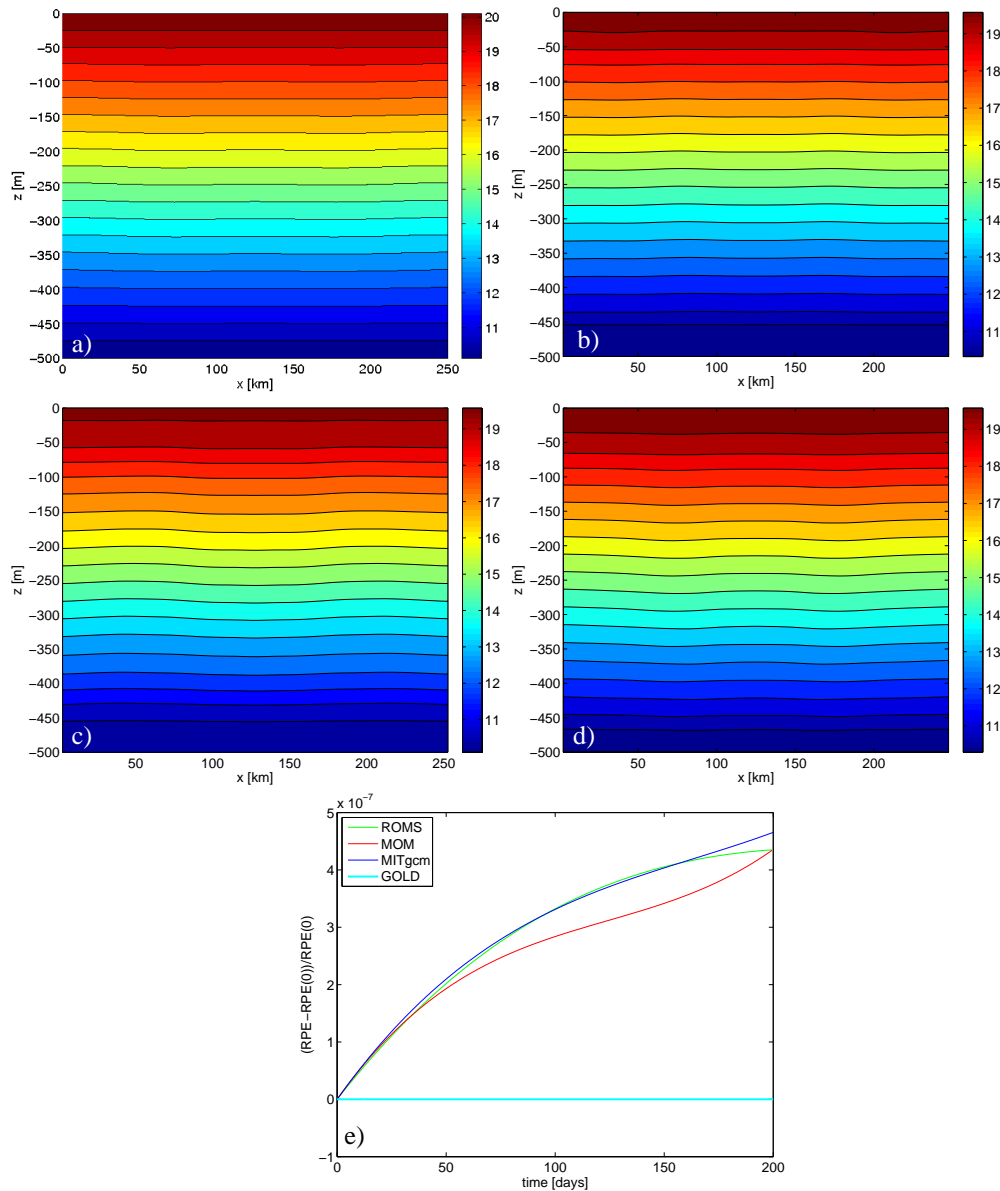


Fig. 12. Temperature after 200 days of simulation for the low amplitude internal waves test case for (a) GOLD (b) ROMS (c) MITgcm and (d) MOM. The contour intervals are set according to the 20 layers used in the GOLD simulation. Panel (e) shows the time evolution of the normalized reference potential energy \overline{RPE} for different codes.

solves most of the mesoscale and some of the sub-mesoscale eddies. The middle grid spacing is $\Delta = 4$ km, which we interpret as mesoscale eddy permitting. The coarsest grid spacing uses $\Delta = 10$ km, which is marginally eddy permitting. Baroclinic and barotropic time steps are set to 200 seconds and 10 seconds, respectively.

Figure 16(a) displays a snapshot of temperature for the 1 km simulation with ROMS at 200 days.

40 km scale eddy structures are evident, reflecting the scale of the deformation radius. Additionally, there are some small scale filamentary features, which are a hint of sub-mesoscale phenomena as discussed by Capet et al. (2008). The temperature in the medium resolution ROMS simulation is shown in Figure 16(b). The small scale structures are no longer apparent at this resolution, and there are fewer eddies. The coarsest grid spacing admits

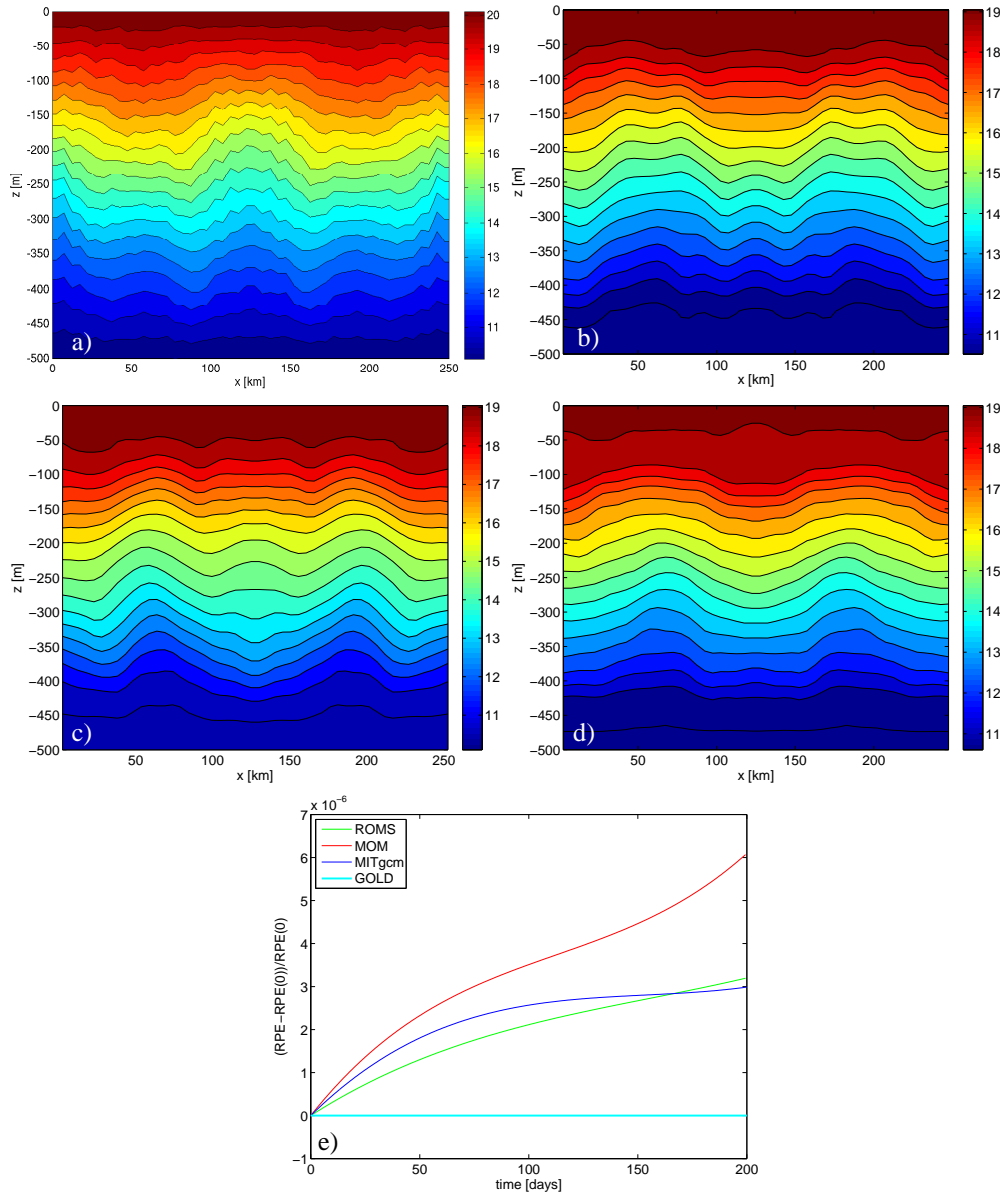


Fig. 13. Temperature field for the high amplitude internal waves test case for (a) GOLD (b) ROMS (c) MITgcm and (d) MOM. The contour intervals are set according to the 20 layers used in the GOLD simulation. Panel (e) shows the time evolution of the normalized reference potential energy \overline{RPE} for different codes.

a relatively weak eddy field, and the horizontal interface between the low and high temperature is blurred [Figure 16(c)].

A suite of MOM and MITgcm simulations were considered with differing lateral viscosities and grid spacings, with a summary given in Table 1. Figure 16(d) shows the temperature of the MITgcm simulations at 200 days using $\nu_h = 20 \text{ m}^2/\text{s}$. The eddies appear well-resolved in the 1 km simulation.

However, the flow is less chaotic than the ROMS simulations, which we attribute to the enhanced viscous dissipation with the $\nu_h = 20 \text{ m}^2/\text{s}$ horizontal viscosity that dissipates the velocity shear and turbulent filaments. The medium and coarse grid simulations are quantitatively similar to the ROMS results [Figures 16(e) and 16(f)]. Baroclinic eddies in the MOM simulations are similar to those in the MITgcm simulations.

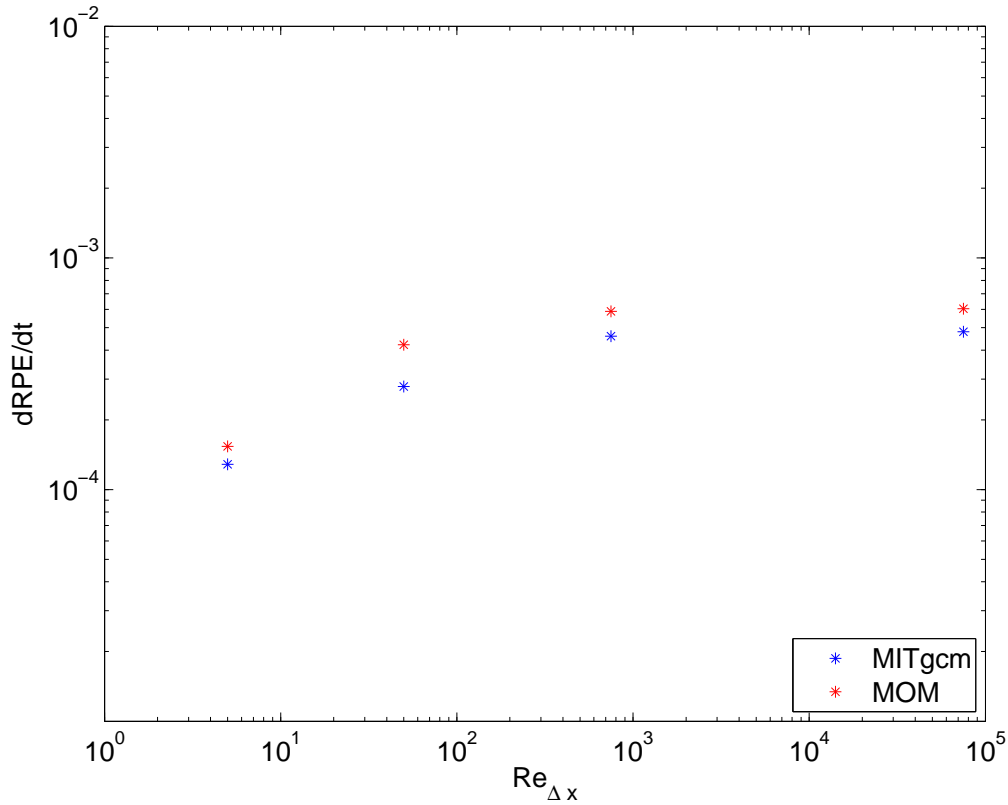


Fig. 14. Rate of change of the reference potential energy [Watts m^{-2}] for MOM and MITGCM as a function grid Reynolds numbers for the high amplitude internal wave test case.

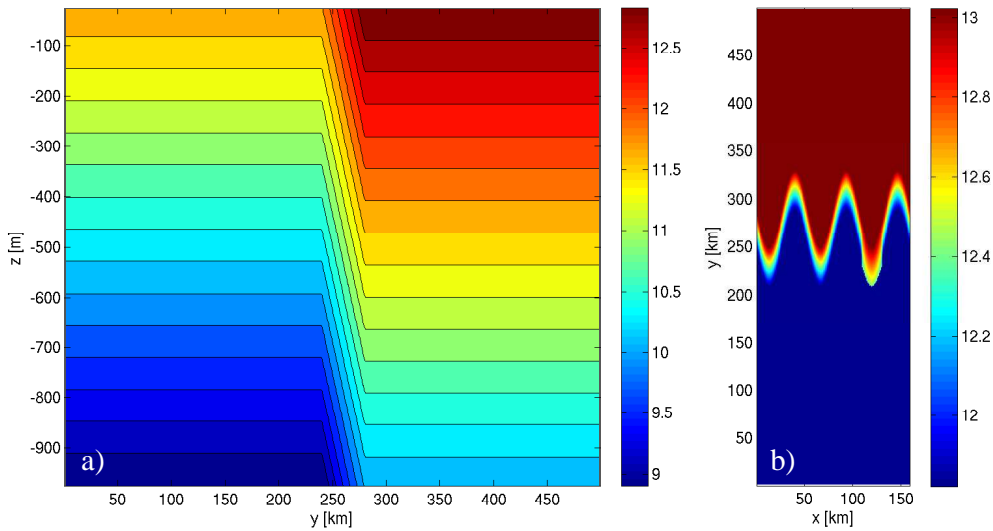


Fig. 15. Left panel: meridional slice through the initial temperature for the baroclinic eddy test case. Right panel: initial surface temperature for the baroclinic eddy test case.

The RPE evolution is now considered in order to measure the degree of spurious diapycnal mixing

in the channel. For the same horizontal viscosity, coarse grid simulations exhibit larger spu-

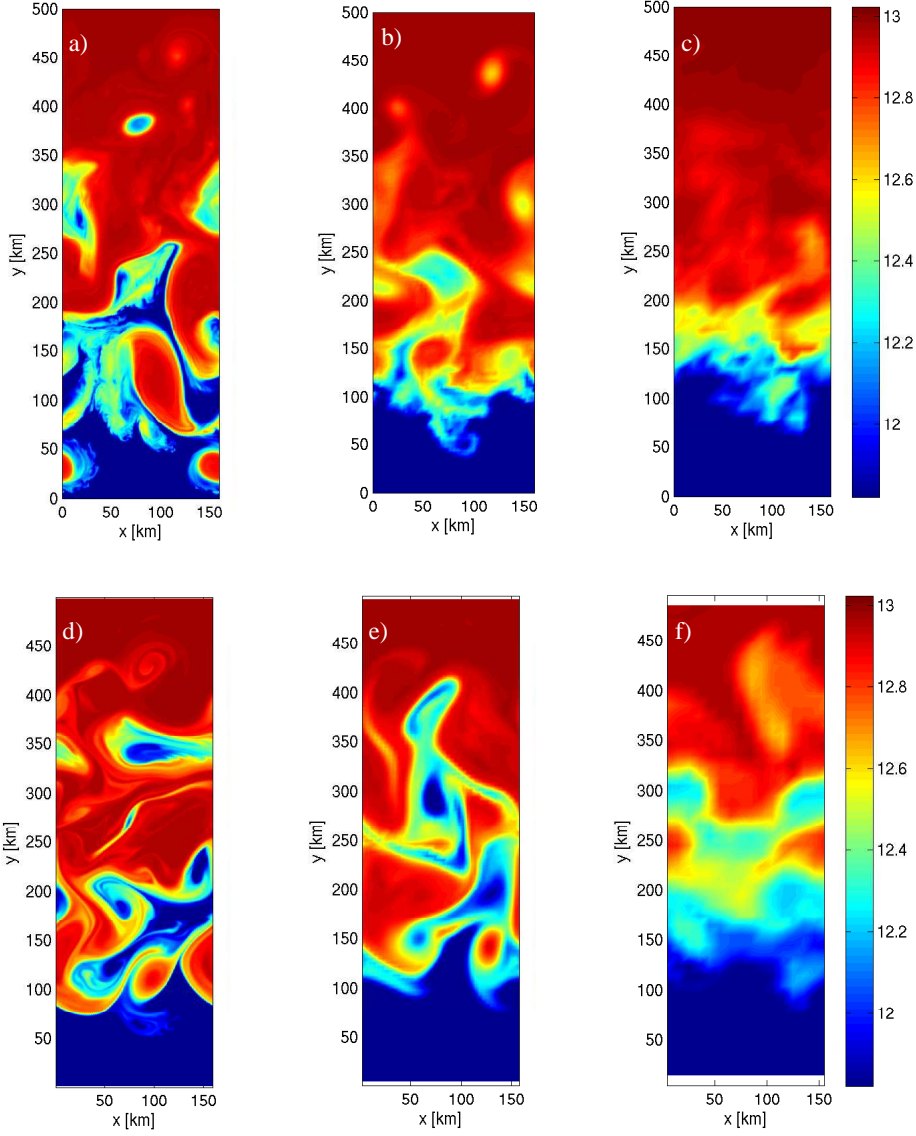


Fig. 16. The top row shows sea surface temperature snapshots at day 200 from the ROMS simulation of baroclinic eddies with horizontal grid spacing of (a) $\Delta = 1$ km; (b) $\Delta = 4$ km; (c) $\Delta = 10$ km. The second row shows temperature snapshots at day 200 from the MITgcm simulations with lateral viscosity of $\nu_h = 20$ m²/s and horizontal grid spacing of (d) $\Delta = 1$ km, (e) $\Delta = 4$ km, (f) $\Delta = 10$ km.

rious mixing than the medium and fine grids (not shown). Figure 17 displays the rate of change of RPE as a function of grid Reynolds number for the MITgcm and MOM simulations. Note that we did not perform all the experiments using MOM since the results are very similar to MITgcm. To compute the grid Re number we use $U_c = \sqrt{2KE}$, as used for the internal wave test case [see equation (9)]. The diagnosed spurious mixing is lowest for

the low Re_Δ , and mixing increases with the grid Reynolds number.

Unlike the other test cases, there is no saturation in the mixing for very high Re_Δ . It is notable that this is the first test case that has rotation. Consequently, tracer variance cascades to the small scales through filamentation, which tends to increase tracer gradients. It was this phenomena that prompted Griffies et al. (2000) to conjecture that eddy simulations are more prone to spu-

Exp	Δ [km]	ν_h [m ² /s]	approx Re_Δ
1	1	5	19
2	1	10	10
3	1	20	5
4	1	200	0.3
5	4	1	406
6	4	5	76
7	4	10	37
8	4	20	18
9	4	200	1.1
10	4	800	0.2
11	10	1	885
12	10	5	182
13	10	10	91
14	10	20	40
15	10	200	2.7
16	10	2000	0.15
17	20	1	1720

Table 1
Experimental setup for the baroclinic eddy test case using MITGCM and MOM. Listed are the experiment numbers, horizontal grid spacings, lateral viscosities, and approximate grid Reynolds number.

rious mixing than non-eddyding. Additionally, as emphasized in the present study, eddyding simulations promote the importance of momentum transport, given the larger contributions from nonlinearities in the momentum equation. Although a quasi-geostrophic eddyding flow sends energy to the large-scales, numerical transport operators in eddyding flows can spuriously create kinetic energy at the small scales. The fact that we do not see saturation of spurious mixing with large grid Reynolds number in the eddyding channel may reflect on these competing cascades in a numerical eddyding simulation.

7. Rationalizing the idealized tests

In general, we found that the horizontal grid Reynolds number is the primary control parameter determining spurious diapycnal mixing in the idealized test cases from Sections 3, 4, 5, and 6. Here, we present an assessment of these results to identify common features and scaling behavior.

To bring the various results together onto a sin-

gle graph, we introduce a non-dimensional parameter defined as

$$\chi \equiv \frac{d(RPE)/dt}{g \delta \rho W_{rms} \Delta z / 2}, \quad (10)$$

where $\delta \rho$ is the initial density difference for the test cases, $d(RPE)/dt$ is the time rate of change for the reference potential energy, and $W_{rms} \Delta z / 2$ is the first order upwind advection in the vertical. We employ W_{rms} , the spatial root-mean square velocity, since it is the scale of noisy vertical velocities. Structurally, χ is like an inverse Peclet number. It could also be interpreted as the fraction of fluid volume that has numerical mixing equivalent to first order upwind. Figure 18 shows χ as a function of grid Reynolds number for the different test cases using the MITGCM simulations. The MOM simulations follow similar behavior (not shown). The dam break and overflow tests have similar magnitude for χ , since both have similar dynamics determined by two-layer flow without rotation. The internal wave and baroclinic eddy tests are stratified, and they too have similar magnitudes. The key point to emphasize here is that all four curves have the same shape. For the high Re_Δ there is a saturation for most of the test cases (except the baroclinic eddy test; see Section 6), and spurious mixing decreases with decreasing Re_Δ when Re_Δ is below 10.

7.1. Treatment of the momentum closure

Since we have concluded that the grid Reynolds number is the governing parameter, we identify here two methods to ensure the grid Reynolds number is sufficiently small to ensure small spurious mixing. The first employs a momentum advection scheme that has dissipation built into the numerical transport operator. As discussed in Section 3.4, ROMS employs just such a scheme, in which the dissipation maintains a grid Reynolds number smaller than two (Shchepetkin and McWilliams, 2005; Marchesiello et al., 2009). As seen from the numerical tests presented thus far, ROMS performed much better than MITGCM and MOM. We therefore consider the ROMS approach highly desirable from the perspective of minimizing the opportunities for the flow to exhibit unphysically large spurious mixing.

The second approach uses a local adaptive momentum closure scheme. This method com-

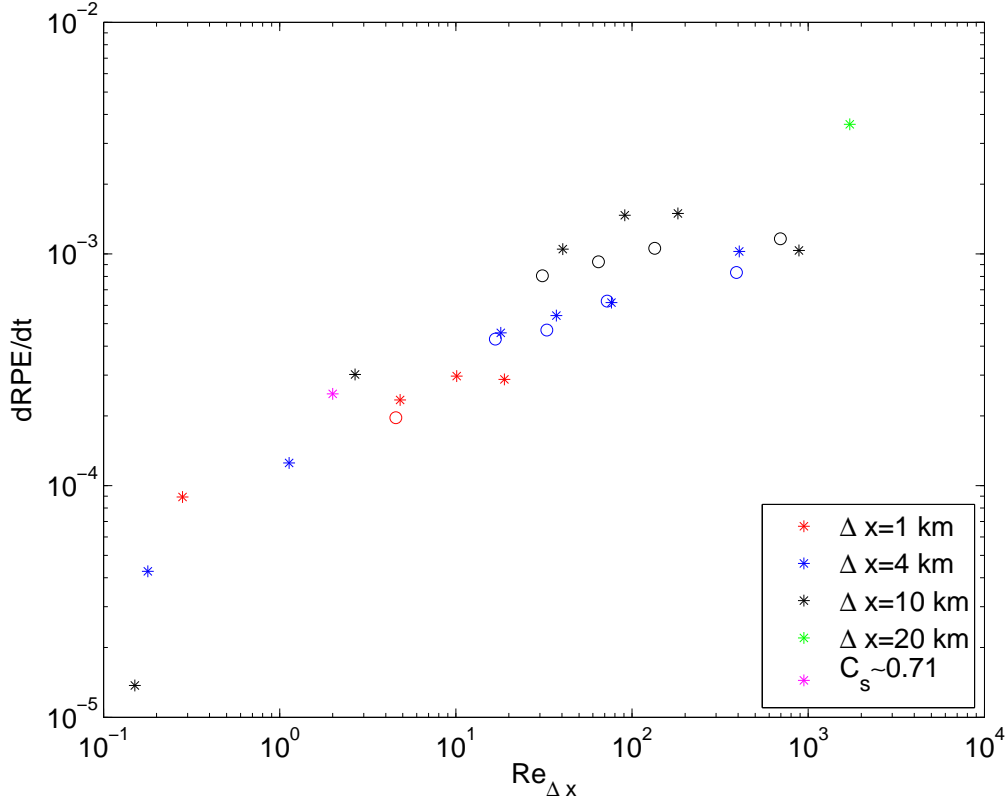


Fig. 17. Rate of change of the RPE [Watts m^{-2}] for MITGCM (star) and MOM (circle) simulations as a function of grid Reynolds number, Re_{Δ} , for the baroclinic eddy test case.

plements that used in ROMS, with the main distinction being that the momentum equation is mathematically closed via the introduction of an explicit friction operator, rather than through incorporating dissipation within the momentum advection scheme. Both approaches can, in principle, be formulated to allow for no larger than a pre-specified grid Reynolds number.

We elaborate a bit more on the adaptive momentum closure approach, as there are options in MITGCM and MOM that allow us to test its utility. Namely, we consider the approach of Smagorinsky (1963) and Smagorinsky (1993), where the Laplacian viscosity is defined according to the grid and flow dependent expression

$$\nu_{SM} = (C_s \Delta)^2 |S|. \quad (11)$$

In this equation, $C_s = \gamma/\pi$ is a non-dimensional Smagorinsky coefficient, S is the deformation rate, and Δ is the grid spacing. For our applications, Δ is the horizontal grid spacing, ν_{SM} sets the lateral viscosity, and γ is the non-dimensional number used in MITGCM and MOM.

Following Griffies and Hallberg (2000), we obtain a scale for the Smagorinsky viscosity by scaling the deformation rate according to a horizontal velocity scale and the grid spacing

$$|S| \sim U/\Delta, \quad (12)$$

thus leading to

$$\nu_{SM} \sim C_s^2 \Delta U. \quad (13)$$

A corresponding grid Reynolds number is given by

$$Re_{\Delta} = \frac{U \Delta}{\nu_{SM}} \sim \frac{1}{C_s^2}. \quad (14)$$

We recommend values aligned with Griffies and Hallberg (2000), who suggest

$$C_s = 1/\sqrt{2}, \quad (15)$$

so that $Re_{\Delta} = 2$.

This value for C_s is far larger than that typically used in large eddy simulations (LES) of 3D isotropic turbulence, in which $C_s \approx 0.17$

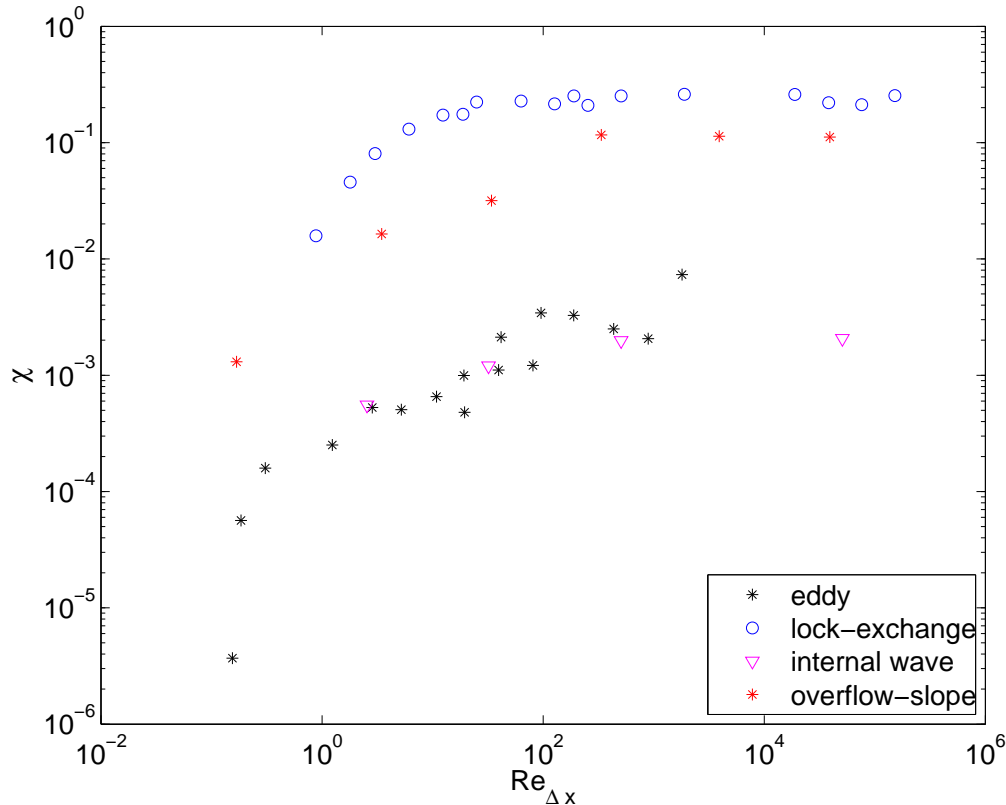


Fig. 18. The non-dimensional mixing parameter χ , defined by equation (10), as a function grid Reynolds numbers, $Re_{\Delta x}$, for all the idealized test cases.

(Smagorinsky, 1993). According to the scaling in equation (14), the corresponding grid Reynolds number would be on the order of $(0.17)^{-2} \approx 35$. As seen from the idealized simulations presented earlier, this large grid Reynolds number would lead to excessive spurious mixing in ocean circulation models. Furthermore, most of the 3D energy containing scales have to be resolved in LES models, whereas ocean circulation models are typically far coarser than that required to resolve a portion of the 3D turbulence cascade. We therefore propose that the larger value suggested by Griffies and Hallberg (2000) is appropriate for ocean circulation models.

To test the utility of the Smagorinsky approach, we perform three additional simulations with the MITgcm using a Laplacian Smagorinsky viscosity with $C_s = 1/\sqrt{2}$ (i.e. $\gamma \sim 2.221$). The first simulation is the dam break using the finest grid spacing of $\Delta z = 1$ m and $\Delta x = 500$ m, along with a nonzero background lateral viscosity of $\nu_h = 10^{-2}$ m²/s. Figure 2(h) shows the result absent the Smagorinsky closure, whereas the temperature

field after 17 hours with the Smagorinsky viscosity is shown in Figure 19(a). The noise at the head of the gravity current seen in Figure 2(h) is significantly reduced with the Smagorinsky scheme. Correspondingly, the spurious numerical mixing is greatly suppressed (magenta point in Fig. 6).

The second test case is the overflow on a slope. Similar to the previous problem, we perform the simulation with Smagorinsky viscosity in addition to the constant background lateral viscosity of $\nu_h = 10^{-2}$ m²/s. Figure 19(b) shows the temperature field when the gravity current reaches the bottom. This simulation can be compared to Figure 9(g) or Figure 9(k). The former has the same background lateral viscosity but no Smagorinsky contribution and the latter has similar grid Reynolds number compared to the simulation with Smagorinsky closure. Once again, the spurious mixing is reduced with use of the Smagorinsky scheme (magenta point in Fig. 10), and the dense water dilution is comparable to ROMS.

The third experiment using the Smagorinsky closure, shown in Figure 19(c), is the baroclinic

eddy test case of the section 6. In contrast to the solution using uniform viscosity [Fig. 16(d)] there are more sub-mesoscale features apparent when using the Smagorinsky closure (white rectangle area in Figure 19(c)). Moreover, the spurious mixing is reduced with use of the Smagorinsky scheme (magenta point in Fig. 17). The nature of these small scale features is quite different than the small scale features seen in the ROMS solution [Fig. 16(a)]. It is not clear whether these structural differences at sub-mesoscale have an impact on the well-resolved mesoscale, nor is it obvious which is more accurate. It remains an open research question how to specify the momentum closure at these resolutions.

All three idealized simulations make a compelling case for the use of adaptive momentum closure to reduce spurious mixing while minimally dissipating the large scale kinetic energy.

8. Global domain test case

So far, we have developed an understanding of spurious mixing in the context of idealized experiments. However, the motivation for understanding spurious mixing arises from the open question of how much spurious diapycnal transport occurs in realistic global ocean models. Here, we extend our analysis to global simulations using MOM and GOLD.

The RPE diagnostic of spurious mixing used throughout this study can only be easily interpreted in the absence of buoyancy forcing and diabatic processes. To use the RPE method in a realistic global model we are thus limited to diagnosing “spin-down” experiments in which a spun-up model state is used as initial conditions. We identify the following three caveats regarding this experimental design for use in diagnosing spurious diapycnal transport.

- (i) The unforced solution is potentially less energetic than the forced solution, and so any associated spurious diapycnal transport may be underestimated.
- (ii) Conversely, the spin-down experiment can in fact lead to a large initial adjustment that introduces more spurious transport than present in the realistic forced simulation. We found this to be the case in the following simulations, but only for the first 5-20 days.
- (iii) To isolate the spurious diapycnal transport

Model	Resolution [degree]	Explicit κ [m ² s ⁻¹]	$\frac{d}{dt}RPE$ [GW]	ΔRPE [GW]
MOM	1	0	336	0
MOM	1	1×10^{-7}	344	8
MOM	1	1×10^{-6}	411	75
MOM	1	1×10^{-5}	1012	676
MOM	1/4	0	1015	0
MOM	1/4	1×10^{-6}	1089	74
MOM	1/4	1×10^{-5}	1701	686
MOM (double Smag.)	1/4	0	675	N/A
GOLD	1	0	107	0
GOLD	1	1×10^{-7}	124	17
GOLD	1	1×10^{-6}	192	85
GOLD	1	1×10^{-5}	656	549
GOLD	1	1×10^{-4}	3819	3712
GOLD	1	Realistic	916	809
GOLD	1/4	0	97	N/A

Table 2

Parameters and results for the global ocean spin-down experiments. The tabulated time rate of change of RPE is averaged over days 20–70 in order to exclude the initial adjustment (Fig. 20) and has been converted to a global work rate, given in gigawatts, using an area of 361×10^{12} m². Vertical diffusivities, κ_d , are given in units of m² s⁻¹. ΔRPE is the change in the RPE tendency from the corresponding simulation with zero explicit diffusivity.

associated with the advection scheme, we remove all vertical and lateral subgrid scale operators from the tracer equation. Doing so exposes the advection operator to enhanced gradients that otherwise are not present in the full simulation. The degree of spurious transport associated with advection may in turn be over-estimated.

Having stated these caveats, we are unaware of a more convenient and robust direct measure of the spurious diapycnal transport within a realistic model configuration using a nonlinear equation of state.

8.1. Model configuration

We consider two representative resolutions using the MOM ocean component of two GFDL coupled models: the nominally 1° grid configuration used in CM2.1 and ESM2M (Delworth et al., 2006; Dunne et al., 2012) and the nominally 1/4° grid

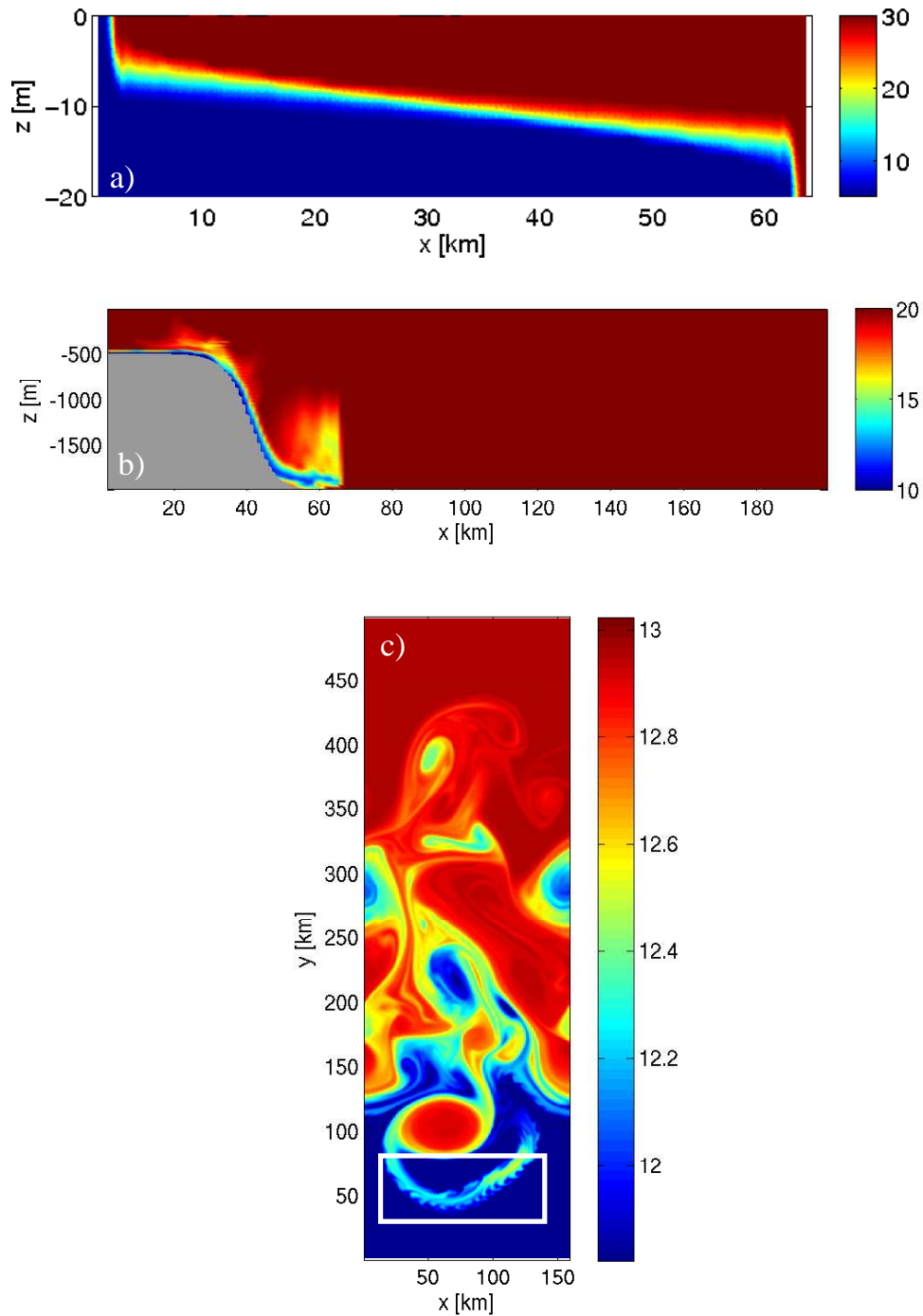


Fig. 19. Simulations with the MITGCM using a constant background lateral viscosity of $\nu_h = 10^{-2} \text{ m}^2/\text{s}$ along with a Smagorinsky viscosity with a non-dimensional coefficient $C_s = 1/\sqrt{2}$. (a) Temperature after 17 hours in the dam break test case. This result should be compared to Figure 2(h), which is run without the Smagorinsky closure. (b) Temperature after 17 hours for the overflow test case. This result should be compared to Figure 9(g), which used the same background lateral viscosity but no Smagorinsky viscosity. (c) Temperature of MITGCM for the 1 km baroclinic eddy test case with a Smagorinsky viscosity, to be compared to Figure 16(d). The white rectangle highlights the enhanced sub-mesoscale structures (see text for more discussion).

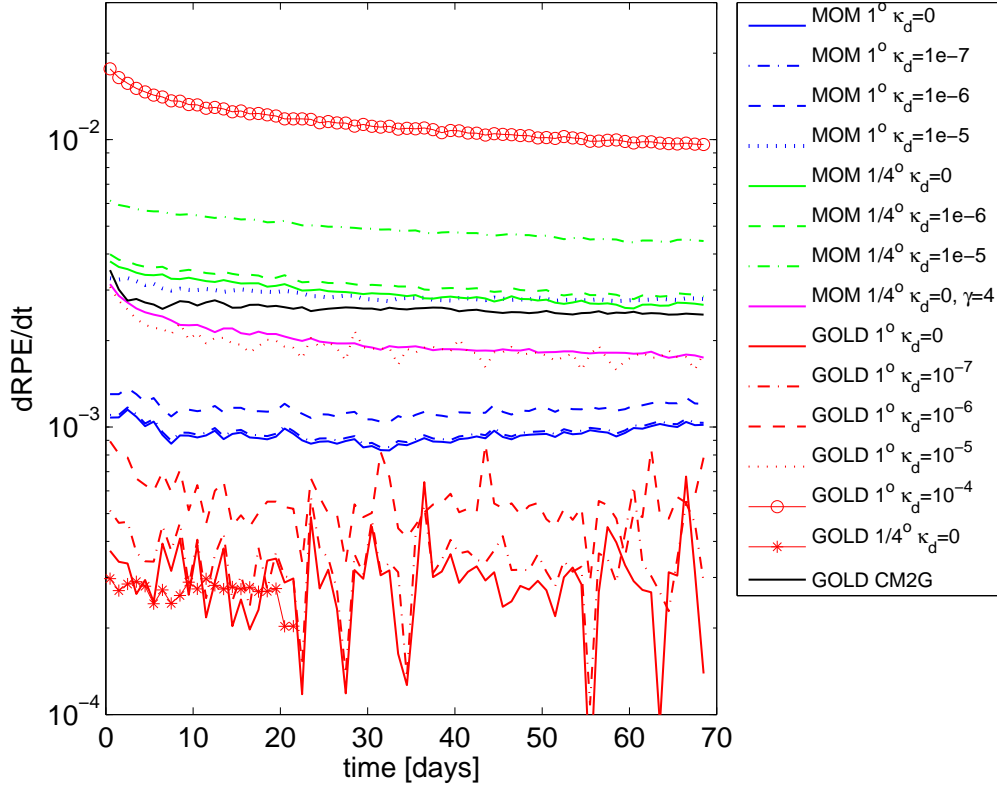


Fig. 20. Time rate of change of RPE for the global models in $W m^{-2}$. Note the initial adjustment induces enhanced mixing in the first 5–20 days.

configuration used in the eddy-permitting CM2.5 (Delworth et al., 2012). As stated above, all surface forcing (buoyancy and wind stress), vertical tracer diffusion, and lateral tracer parameterizations are disabled in the spin-down experiments including adiabatic parameterizations like GM parameterization (Gent and McWilliams, 1990). Otherwise, the ocean configurations are consistent with those used in the fully coupled models, in particular the details of identical momentum closure.

The most relevant aspect of these configurations for this discussion is that both models use Smagorinsky-based momentum closures. Both 1° and $1/4^\circ$ models use $C_s \approx 0.6366$ ($\gamma = 2$) in a bi-harmonic operator, with the 1° also using a prescribed spatially dependent Laplacian background. The biharmonic Smagorinsky settings correspond to recommendations from Griffies and Hallberg (2000). For comparison, and to serve as a benchmark, a similarly configured 1° GOLD simulation is run in spin-down mode, as well as with various values of explicit vertical diffusion. In addition, we also performed $1/4^\circ$ eddy permit-

ting GOLD simulations to investigate the effect of resolution within the isopycnal model.

8.2. Analysis method

In these global configurations, the RPE diagnostic becomes more difficult to compute, in both model classes, due to the nonlinearity of the equation of state and the Boussinesq approximation. Cabbeling and thermobaricity (McDougall, 1987; IOC et al., 2010) modify the mass of the ocean in the MOM simulations (Boussinesq models conserve volume and not mass), with mass generally increasing since density generally increases with cabbeling and thermobaricity. For the GOLD simulations, because the numerical mixing is along isopycnal, spurious thermobaricity does not contribute to the diapycnal transport (see Section A.27 of IOC et al., 2010). However, there is spurious cabbeling, which again produces a mass source. A mass source can lead to a signal in the RPE calculation that is dependent on the arbitrary zero point measuring the potential energy. We correct

this signal by shifting to a vertical coordinate centered at the instantaneous center of volume, to render the RPE calculation frame invariant. We detail this method in Appendix A.

8.3. Results and interpretation

The time rate of change of corrected RPE is shown in Figure 20, for all the global spin-down experiments. The corresponding global work in gigawatts, averaged over the last 50 days, is listed in Table 2. The solid-red line shows the RPE for the GOLD spin down calculation without explicit vertical or lateral mixing. GOLD exhibits a spurious potential energy source due to the cabbeling associated with numerical mixing along isopycnals. This level of numerical cabbeling amounts to about 107 GW, which is approximately one quarter the estimated physical energy change due to mixing by lateral processes, which is of order 400GW in a global model (Gnanadesikan et al., 2005). We believe that the amount of spurious energy source in GOLD is due to the pseudo-second order piecewise-linear method (PLM) for tracer advection, which is fairly diffusive.

The total mixing work in GOLD increases monotonically as explicit diapycnal diffusion increases, but only with a power of 0.8 instead of 1. We therefore suspect that the spurious numerical cabbeling is a function of state and explicit mixing, which indeed is consistent with our fundamental understanding of cabbeling (McDougall, 1987). Thus we cannot readily partition the spurious potential energy source into spurious diapycnal mixing and spurious cabbeling.

We also note that the noise in the time series (Figure 20) is only significant for low values of explicit diapycnal mixing in GOLD ($\kappa_d = 0, 10^{-7} \text{ m}^2\text{s}^{-1}$), but rapidly becomes insignificant for models where the diagnosed spurious work is of order 10^{-3} Wm^{-2} or greater. We consider the amplitude of this noise to be an error estimate for our work measurements, namely of order $3 \times 10^{-4} \text{ Wm}^{-2}$.

The 1° and $1/4^\circ$ MOM solutions are shown in blue and green respectively in Figure 20. In agreement with Griffies et al. (2000), the eddy-permitting solution shows more spurious potential energy gain (i.e., work) than the non-eddy-permitting simulation. The diagnosed spurious work in the 1° and $1/4^\circ$ MOM models amount to 336 GW and 1015 GW, respectively. As for GOLD,

the diagnosed work in MOM increases monotonically with explicit diapycnal diffusion.

The various MOM simulations show clear and remarkably consistent sensitivities to changing κ_d from 0 to $10^{-6} \text{ m}^2/\text{s}$ and yet have levels of spurious work that are much larger than these changes. One might be tempted to argue that if a sensitivity to a small change in explicit diffusivity can be detected, then the spurious mixing might be smaller than this explicit diffusivity. However, as illustrated in Fig. 20 and Table 2 this is not the case in realistic global models. The quantitative similarities of the sensitivity of RPE changes to the addition of explicit diapycnal diffusion for the various models, listed in the last column of Table 2, strongly suggests that the spurious transport and the work from explicit diffusion add almost linearly.

The time derivative of RPE cannot be directly compared to the actual work needed to sustain mixing (e.g. as in Munk and Wunsch (1998)) because density changes in geographically separated water parcels of similar density can magnify the change in RPE; this is the same reason that the diagnosed spurious diffusivity of Griffies et al. (2000) is questionable in global instances. Instead, using this metric on a model with “realistic” parameterized mixing and relatively small numerical mixing can provide a rough estimate to evaluate whether the numerical mixing is significant. A diabatic spin-down diagnostic of GOLD with “realistic” parameterizations of internal-tide driven mixing, shear-instability, etc. (Dunne et al., 2012) yields 916 GW change in RPE. After correcting for the 107 GW of mixing that this configuration gives with no explicit diapycnal mixing (perhaps due to numerical cabbeling) gives an estimate of 809 GW for the real work diagnosed by this metric, which can be used as a benchmark (potentially an overestimate) to gauge the significance of the spurious work in the other models. The spurious work in the 1° MOM spin-down (336 GW) is of order one quarter (28%) of the notional real work we estimate from GOLD (809 GW). However, if we were able to account for the part of spurious work due to spurious cabbeling, the ratio of spurious mixing in 1° MOM to real dissipation would be reduced. The spurious work in the $1/4^\circ$ MOM model (1015 GW) is of order 1.1 times that of the notional real work found in GOLD.

Following our conclusions from the idealized experiments shown previously, and in agreement with Griffies et al. (2000), we find that decreas-

ing the grid Reynolds number by increasing the Smagorinsky coefficient by a factor of two significantly reduces the diagnosed spurious work in the $1/4^\circ$ MOM calculation (magenta line, 675 GW) by about a third, so that the spurious work is around 70% that of the notional real work in the GOLD simulation.

While the spurious potential energy source increases in MOM when refining the grid resolution from 1° to $1/4^\circ$, the spurious cabbeling in GOLD is mostly unchanged, reducing slightly from 107 GW in 1° GOLD to 97 GW in $1/4^\circ$ GOLD. We would expect the along isopycnal numerical mixing to be reduced with refined resolution. The apparent lack of convergence could indicate enhanced gradients in the refined grid spacing simulation. However, the $1/4^\circ$ GOLD simulation was unstable after 20 days in the absence of lateral parameterizations. Thus, we are not confident that the diagnosed spurious energy in the first 20 days of the $1/4^\circ$ GOLD simulation is meaningful.

9. Discussion and conclusions

We have diagnosed spurious dianeutral transport in four numerical ocean codes by means of the Winters et al. (1995) reference potential energy (RPE) method. The experiments focused on different dynamical processes, but revealed a common dependence on the lateral grid Reynolds number, $Re_\Delta = U \Delta / \nu$, with U an appropriately defined horizontal velocity scale, Δ the horizontal grid scale, and ν the lateral viscosity.

9.1. Spurious mixing in idealized simulations

Although we found a common dependence of spurious mixing on grid Reynolds number, across the range of experiments, we did not find a conclusive scaling that could predict *a priori* the absolute degree of spurious mixing. The use of a grid Reynolds number below 10 is a sensible and universal recommendation to avoid the saturation level of spurious mixing, but this would not guarantee that the remaining spurious mixing would be insignificant.

One case where the saturation was not evident was the baroclinic eddy channel experiment. This different behavior could be due to several reasons that we did not test in this paper.

- (i) The existence of a turbulent cascade in the channel case, which is not present in the other cases, may alter the scaling behavior.
- (ii) We might be using the wrong velocity scale for calculating the grid Reynolds number (e.g. either the ageostrophic flow scale or a measure of the amplitude of grid-scale noise might be better choices).
- (iii) A universal scaling may not exist.

Although the internal wave case followed the same saturation pattern as the other 2D adjustment problems, the relative degree of spurious mixing (Figure 18) was more in-line with the 3D baroclinic eddy case. We suggested in Section 7 that the effective inverse Peclet number (equation (10)) provides a useful measure of the volumetric fraction of the fluid that is experiencing first-order advection errors (i.e., a diffusivity of order $W_{rms} \Delta z$) due to the flux limiters. For a stratified fluid, the extrema that are limited are predominately at the top and bottom boundaries while in the unstratified problems, the limiters act only in the interior where the flow is transporting a discontinuity in the tracer fields. The issue of what determines the absolute levels of mixing, and whether a universal model of spurious mixing can be found, remains an open question.

In our experiments, we did not thoroughly examine the role of different tracer advection schemes, but we did find common degrees of mixing between two similar models (MITGCM and MOM) which each had very different schemes. We have no doubt that the use of a first order upwind tracer advection scheme would yield far more spurious mixing than any that we diagnosed here. Our results suggest that an advection scheme needs only be of sufficient accuracy (say third order) before the grid-scale noise in velocity becomes the dominant cause of spurious dianeutral transport.

9.2. Spurious dianeutral transport in global simulations

In our examination of the realistic global models, we found significant spurious sources of potential energy, indicating significant spurious dianeutral transport. Not all of this energy is due to spurious dianeutral mixing, even though it is all spurious. In particular, the signal in GOLD contains a contribution from spurious cabbeling as-

sociated with numerical mixing along isopycnals. The MOM simulation has a contribution from both spurious cabbeling and spurious thermobaricity, again due to numerical mixing in the epineutral direction.

GOLD exhibited a nontrivial amount of this spurious work (107 GW). The use of the quasi-second order piecewise-linear method (PLM) is a likely source of this spurious mixing, since PLM is more diffusive than any of the higher order schemes used in the other models used here.

The spurious work diagnosed in the MOM-based climate models was also larger than we had expected. Our results suggest that spurious processes in the 1° model do as much as a quarter of the work done by tides and winds in the realistic configuration, and that in the $1/4^\circ$ model, spurious processes do as much as 110% of the notional real work. However, consistent with our understanding developed from the idealized experiments, we were able to reduce the spurious work down to 70% by increasing the viscous dissipation. We expect that further refinements in the momentum closure will further bring down the spurious work. Whether this reduction in spurious work can be done without compromising the fidelity of the circulation (i.e., over-dissipating the eddy kinetic energy) remains to be seen. The main lesson is that this spurious work diagnostic should play a key role in ocean climate model development.

9.3. Concerning momentum closure

Griffies et al. (2000) and Legg et al. (2008) suggest that sufficient dissipation of momentum is a requirement to limit spurious dianeutral transport. Here, we found that spurious dianeutral mixing saturates above a lateral grid Reynolds number of order 20–100. For smaller grid Reynolds numbers, the spurious mixing is reduced in direct proportion to the reduction in the grid Reynolds number. Jochum et al. (2008) suggest that optimal viscosity should be large enough to suppress the numerical instabilities on the grid scale (i.e. grid noise) but small enough to allow the general circulation model to reproduce sharp fronts and mesoscale features where the resolution permits. We found that increasing a uniform viscosity reduces the numerical mixing but also dissipates vertical shear and kinetic energy, whereas an adaptive momentum closure can better optimize the level of numer-

ical mixing and the dissipation of kinetic energy. As Jochum et al. (2008) concluded, a systematic exploration of the dependence between viscosity, topography, resolution and grid noise is required.

A major conclusion from this study is the importance of momentum dissipation for the purpose of reducing spurious dianeutral transport to physically negligible levels. This conclusion is based on observing that the ROMS simulations typically yielded the least spurious mixing amongst the non-isopycnal models considered in the idealized test cases. This reduced spurious dianeutral transport is due to the nonlinear momentum advection scheme of Shchepetkin and McWilliams (1998) that locally adapts momentum closure at the grid-scale to reduce grid scale energy in the velocity field. An alternative method was illustrated in the MITGCM and MOM, in which an adaptive lateral viscosity scheme due to Smagorinsky (1963, 1993) was found to drastically reduce spurious dianeutral mixing.

Hence, the major conclusion of this paper is that lateral momentum closure, as realized either through the momentum advection operator or through a dissipation operator, plays a leading role in the control of spurious dianeutral transport. This conclusion follows from the need to reduce kinetic energy at or near the grid scale, with such grid scale energy appearing especially in simulations where nonlinear momentum transport is important; i.e., eddying flows or flows undergoing a nonlinear adjustment such as a dam break or overflow. Too much kinetic energy at or near the grid scale leads, through the continuity equation, to large vertical velocities with high spatial variability. Such vertical velocities wreak havoc on tracer advection schemes, thus necessitating the frequent use of low order dissipative flux limiters to retain monotonicity, which in turn contributes to unphysically large spurious dianeutral mixing.

Based on the results from the ROMS dissipative momentum advection scheme, and the Smagorinsky scheme in MITGCM and MOM, it may be possible to realize simulations in non-isopycnal models with reduced spurious dianeutral transport, hopefully without overly compromising the flow kinetic energy. At present, however, this goal remains to be realized in eddy-permitting global ocean climate models. We intend to pursue research addressing this issue in the near future.

Acknowledgements

We thank Whit Anderson and Matthew Harrison for assistance with the global simulations. We also thank Sonya Legg, John P. Dunne, Anthony Rosati, and two anonymous reviewers for their constructive criticisms. We thank Markus Jochum for pointing out the confusion that could arise from the inconsistency between the work diagnosed by the RPE metric and well known solutions for the physical energy requirements for mixing. Rüdiger Gerdes emphasized the importance of momentum dissipation for reducing spurious di-neutral transport during a talk at a 2007 CLIVAR ocean modelling workshop in Bergen, Norway (www.clivar.org/organization/wgomd/wgomd.php).

Appendix A. Calculating the reference potential energy

The reference potential energy (RPE), which is used as a diagnostic throughout this paper, is the potential energy of the adiabatically sorted state. It is the same potential energy that is used to define the available potential energy (APE) which is that part of the total potential energy (PE) that is available to the dynamical system:

$$\begin{aligned} APE &= PE - RPE \\ &= \iiint g \rho z dV - \iiint g \rho^* z dV \end{aligned} \quad (\text{A.1})$$

where ρ^* indicates the density in the sorted state that has the minimal potential energy that can be reached adiabatically.

The absolute values of RPE and PE are dependent on the frame chosen to reference the zero point of potential energy. APE is frame invariant because it is the difference of two potential energies, but it is usually unstated that those energies should be calculated in the same frame of reference. However, the issue of reference frame concerns us here because we are interested in the rate of change of the RPE itself which is, unfortunately, subject to the arbitrary choice of reference frame.

We partition the *in situ* density into a mean, $\bar{\rho}$, and perturbation, ρ' , and choose a reference vertical position relative to the center of volume, \bar{z} , as defined according to

$$\bar{\rho} \equiv \frac{1}{V} \iiint \rho dV \quad (\text{A.2})$$

$$\bar{z} \equiv \frac{1}{V} \iiint z dV. \quad (\text{A.3})$$

The potential energy integral can then be rewritten as

$$\begin{aligned} PE &= \iiint g \rho z dV \\ &= \iiint g (\bar{\rho} + \rho') (\bar{z} + z') dV \\ &= g \bar{\rho} \bar{z} \iiint dV + g \bar{z} \underbrace{\iiint \rho' dV}_{=0} \\ &\quad + g \bar{\rho} \underbrace{\iiint z' dV}_{=0} + g \iiint \rho' z' dV. \end{aligned} \quad (\text{A.4})$$

The second and third terms, on the right hand side, vanish due to the definition of $\bar{\rho}$ and \bar{z} . The last term is the part of the potential energy that evolves as the density distribution evolves and, when applied to the sorted state ρ^* , will change due to mixing. The first term is frame dependent. If mass and volume are conserved, the first term will not change with time and so we can safely measure RPE rates of change. However, using a nonlinear equation of state in a Boussinesq model, mass is not conserved; numerical mixing (both epineutral and di-neutral) leads to cabbeling and a general increase in the mass of the system. Thus, when we analyze the realistic GCMs that use a nonlinear equation of state, we adjust the background potential energy integrals by the first term so that we are only seeing contributions from the last term. Specifically, we use

$$RPE = g \iiint (\rho^*)' z' dV \quad (\text{A.5})$$

in the analysis of the global models.

A second detail concerns the method of finding the adiabatically adjusted state, ρ^* . The properly sorted state is defined such that the static stability of any two vertically adjacent parcels be non-negative. Static stability is a function of pressure and the [hydrostatic] pressure is the integral of density over all water parcels above any given position. A simple algorithm to sort density is as follows: starting at a zero pressure, find the lightest possible water parcel by evaluating the equation of state for every water parcel at this zero pressure. Distribute this parcel over the area of the ocean

and integrate down for the pressure of the next level. Then find the lightest parcel among the remaining water parcels by evaluating the density at this local pressure.

This algorithm is a "selection sort" which is an order N^2 calculation, where N is the number of model grid cells. It is computationally very expensive because each operation requires the evaluation of the nonlinear equation of state for seawater (TEOS-10 is a 48 term expression for density). We used this full (expensive) algorithm to test a simpler approximate algorithm in which the sorting uses ρ_{2000} , the potential density referenced to 2000 dbars. Only one evaluation of the equation of state needs to be made for each point, and a conventional $N \log(N)$ sort be applied to ρ_{2000} itself. We find empirically (using a sub-sampled data set) that although the sorted state is not strictly statically stable, the calculation of the rate of change of RPE (using the in-situ density) is accurate to 1%, or better. For a 1° data set, the full algorithm cost 24 hours in Matlab on a 2.67GHz Xeon cpu while the ρ_{2000} approximate method takes 3 seconds. A more efficient $N \log(N)$ sort that uses the non-linear equation of state would cost somewhere between the two, but was not implemented once the accuracy of the approximate sort was deemed sufficient for the calculation presented in this paper.

References

- Adcroft, A., Campin, J., 2004. Rescaled height coordinates for accurate representation of free-surface flows in ocean circulation models. *Ocean Modelling* 7, 269–284.
- Adcroft, A., Hallberg, R., Harrison, M., 2008. A finite volume discretization of the pressure gradient force using analytic integration. *Ocean Model.* 22, 106–113.
- Adcroft, A., Hill, C., Marshall, J., 1997. Representation of Topography by Shaved Cells in a Height Coordinate Ocean Model. *Monthly Weather Review* 125, 2293–2315.
- Anderson, D. A., Tannehill, J. C., Pletcher, R. H., 1984. *Computational Fluid Mechanics and Heat Transfer*. McGraw-Hill Book Company.
- Benjamin, T. B., 1968. Gravity currents and related phenomena. *J. Fluid Mech.* 31, 209–248.
- Bryan, K., Manabe, S., Pacanowski, R. C., 1975. A global ocean-atmosphere climate model. Part II. The oceanic circulation 5, 30–46.
- Burchard, H., Rennau, H., 2008. Comparative quantification of physically and numerically induced mixing in the ocean models. *Ocean Modell.* 20, 293–311.
- Capet, X., McWilliams, J. C., Molemaker, M. J., Shchepetkin, A. F., 2008. Mesoscale to Submesoscale Transition in the California Current System. Part I: Flow Structure, Eddy Flux, and Observational Tests. *Journal of Physical Oceanography* 38, 29–43.
- Colella, P., Woodward, P. R., Sep. 1984. The Piecewise Parabolic Method (PPM) for Gas-Dynamical Simulations. *Journal of Computational Physics* 54, 174–201.
- Daru, V., Tenaud, C., Jan. 2004. High order one-step monotonicity-preserving schemes for unsteady compressible flow calculations. *Journal of Computational Physics* 193, 563–594.
- Delworth, T. L., Broccoli, A. J., Rosati, A., Stouffer, R. J., Balaji, V., Beesley, J. A., Cooke, W. F., Dixon, K. W., Dunne, J., Dunne, K. A., Durachta, J. W., Findell, K. L., Ginoux, P., Gnanadesikan, A., Gordon, C., Griffies, S. M., Gudgel, R., Harrison, M. J., Held, I. M., Hemler, R. S., Horowitz, L. W., Klein, S. A., Knutson, T. R., Kushner, P. J., Langenhorst, A. L., Lee, H.-C., Lin, S., Lu, L., Malyshev, S. L., Milly, P., Ramaswamy, V., Russell, J., Schwarzkopf, M. D., Shevliakova, E., Sirutis, J., Spelman, M., Stern, W. F., Winton, M., Wittenberg, A. T., Wyman, B., Zeng, F., Zhang, R., 2006. GFDL's CM2 global coupled climate models - Part 1: Formulation and simulation characteristics 19, 643–674.
- Delworth, T. L., Rosati, A., Anderson, W., Adcroft, A. J., Balaji, V., Benson, R., Dixon, K., Griffies, S. M., Lee, H.-C., Pacanowski, R. C., Vecchi, G. A., Wittenberg, A. T., Zeng, F., Zhang, R., 2012. Simulated climate and climate change in the GFDL CM2.5 high-resolution coupled climate model submitted.
- Dunne, J. P., John, J. G., Hallberg, R. W., Griffies, S. M., Shevliakova, E. N., Stouffer, R. J., Krasting, J. P., Sentman, L. A., Milly, P. C. D., Malyshev, S. L., Adcroft, A. J., Cooke, W., Dunne, K. A., Harrison, M. J., Levy, H., Samuels, B. L., Spelman, M., Winton, M., Wittenberg, A. T., Phillips, P. J., Zadeh, N., 2012. GFDLs ESM2 global coupled climate-carbon Earth System Models Part I: Physical formulation and baseline simulation characteristics. *Journal of Climate* submitted.
- Gent, P. R., McWilliams, J. C., 1990. Isopycnal

- mixing in ocean circulation models. *J. Phys. Oceanogr.* 20, 150–155.
- Getzlaff, J., Nurser, G., Oschlies, A., 2010. Diagnostics of diapycnal diffusivity in z-level ocean models part I: 1-Dimensional case studies. *Ocean Modelling* 35, 173–186.
- Gnanadesikan, A., Slater, R. D., Swathi, P. S., Vallis, G. K., Jul. 2005. The Energetics of Ocean Heat Transport. *Journal of Climate* 18, 2604–2616.
- Gregg, M., Sanford, T., Winkel, D., 2003. Reduced mixing from the breaking of internal waves in equatorial waters. *Nature* 422, 513–515.
- Griffies, S. M., 2004. *Fundamentals of Ocean Climate Models*. Princeton University Press, Princeton, USA, 518+xxxiv pages.
- Griffies, S. M., 2009. *Elements of MOM4p1: GFDL Ocean Group Technical Report No. 6*. NOAA/Geophysical Fluid Dynamics Laboratory, Princeton, USA, 444 pp.
- Griffies, S. M., Hallberg, R. W., 2000. Biharmonic Friction with a Smagorinsky-Like Viscosity for Use in Large-Scale Eddy-Permitting Ocean Models. *Mon. Wea. Rev.* 128, 2935–2946.
- Griffies, S. M., Pacanowski, R. C., Hallberg, R. W., 2000. Spurious Diapycnal Mixing Associated with Advection in a z-Coordinate Ocean Model. *Mon. Wea. Rev.* 128, 538–564.
- Haidvogel, D. B., Beckmann, A., 1999. *Numerical ocean circulation modeling*. Imperial College Press.
- Hallberg, R., Adcroft, A., 2009. Reconciling estimates of the free surface height in Lagrangian vertical coordinate ocean models with mode-split time stepping. *Ocean Model.* 29, 15–26.
- Hill, C., Ferreira, D., Campin, J. M., Marshall, J., Abernathy, R., Barrier, N., 2011. Controlling spurious diapycnal mixing in eddy-resolving high-coordinate ocean models—insights from virtual deliberate tracer release experiments. *Ocean Model.* submitted.
- Ilicak, M., Legg, S., Adcroft, A., Hallberg, R., 2011. Dynamics of a dense gravity current flowing over a corrugation. *Ocean Model.* accepted.
- Ilicak, M., Özgökmen, T. M., Özsoy, E., Fischer, P. F., 2009. Non-hydrostatic modeling of exchange flows across complex geometries. *Ocean Model.* 29, 159–175.
- IOC, SCOR, IAPSO, 2010. *The international thermodynamic equation of seawater-2010: calculation and use of thermodynamic properties*. Intergovernmental Oceanographic Commission, Manuals and Guides No. 56, UNESCO, available from <http://www.TEOS-10.org>, 196pp.
- Iudicone, D., Madec, G., McDougall, T. J., 2008. Water-mass transformations in a neutral density framework and the key role of light penetration 38, 1357–1376.
- Jackson, L., Hallberg, R., Legg, S., 2008. A Parameterization of Shear-Driven Turbulence for Ocean Climate Models. *J. Phys. Oceanogr.* 38, 1033–+.
- Jochum, M., Danabasoglu, G., Holland, M., Kwon, Y.-O., Large, W. G., Jun. 2008. Ocean viscosity and climate. *J. Geophys. Res.* 113, C06017.
- Klocker, A., McDougall, T. J., 2010. Influence of the nonlinear equation of state on global estimates of diapycnal advection and diffusion. *J. Phys. Oceanogr.* 40, 1690–1709.
- Kunze, E., Firing, E., Hummon, J. M., Chereskin, T. K., Thurnherr, A. M., 2006. Global Abyssal Mixing Inferred from Lowered ADCP Shear and CTD Strain Profiles. *Journal of Physical Oceanography* 36, 1553–1576.
- Kunze, E., Sanford, T. B., 1996. Abyssal mixing: where it is not. *J. Phys. Oceanogr.* 26, 2286–2296.
- Large, W. G., McWilliams, J. C., Doney, S. C., 1994. Oceanic vertical mixing: A review and a model with a nonlocal boundary layer parameterization. *Rev. Geophys.* 32, 363–403.
- Leclair, M., Madec, G., 2011. z-Coordinate, an Arbitrary Lagrangian-Eulerian coordinate separating high and low frequency motions. *Ocean Model.* 37, 139–152.
- Ledwell, J. R., St-Laurent, L., Girton, J., Toole, J., 2011. Diapycnal mixing in the Antarctic Circumpolar Current. *Journal of Physical Oceanography* 41, 241–246.
- Ledwell, J. R., Watson, A. J., Law, C. S., 1993. Evidence for slow mixing across the pycnocline from an open-ocean tracer-release experiment. *Nature* 364, 701–703.
- Lee, M.-M., Coward, A. C., Nurser, A. G., 2002. Spurious diapycnal mixing of deep waters in an eddy-permitting global ocean model 32, 1522–1535.
- Legg, S., Briegleb, B., Chang, Y., Chassignet, E. P., Danabasoglu, G., Ezer, T., Gordon, A. L., GriñĆes, S. M., Hallberg, R. W., Jackson, L., Large, W., Özgökmen, T. M., Peters, H., Price, J., Riemenschneider, U., Wu, W., Xu, X., Yang, J., 2009. Improving oceanic overiñĆow representation in climate models: The Gravity Current Entrainment Climate Process Team 90, 657–670.
- Legg, S., Hallberg, R. W., Girton, J. B., 2006. Comparison of entrainment in overflows simulated

- by z-coordinate, isopycnal and non-hydrostatic models. *Ocean Model.* 11, 69–97.
- Legg, S., Jackson, L., Hallberg, R. W., 2008. Eddy-resolving modeling of overflows. In *Ocean Modeling in an Eddy Regime*, Geophysical Monograph 177, M. W. Hecht, and H. Hasumi, eds., Washington, DC, American Geophysical Union, 63–82.
- Lin, S., 2004. A “Vertically Lagrangian” Finite-Volume Dynamical Core for Global Models. *Monthly Weather Review* 132, 2293–2307.
- Maqueda, M. M., Holloway, G., 2006. Second-order moment advection scheme applied to arctic ocean simulation. *Ocean Modelling* 14, 197–221.
- Marchesiello, P., Debreu, L., Couvelard, X., 2009. Spurious diapycnal mixing in terrain-following coordinate models: The problem and a solution. *Ocean Modelling* 26, 156–169.
- Margolin, L., Smolarkiewicz, P., 1998. Antidiffusive velocities for multipass donor cell advection. *SIAM J. Sci. Comput.* 20, 907–929.
- Marsh, R., 2000. Cabbelling due to isopycnal mixing in isopycnic coordinate models. *Journal of Physical Oceanography* 30, 1757–1775.
- Marshall, J., Adcroft, A., Hill, C., Perelman, L., Heisey, C., 1997. A finite-volume, incompressible Navier Stokes model for studies of the ocean on parallel computers. *J. Geophys. Res.* 102, 5753–5766.
- McDougall, T. J., 1987. Thermobaricity, cabbelling, and water-mass conversion. *Journal of Geophysical Research* 92, 5448–5464.
- Merryfield, W. J., Holloway, G., 2003. Application of an accurate advection algorithm to sea-ice modelling 5, 1–15.
- Munk, W., Wunsch, C., 1998. Abyssal recipes II: Energetics of tidal and wind mixing 45, 1977–2010.
- Özgökmen, T. M., Iliescu, T., Fischer, P. F., 2009. Large eddy simulation of stratified mixing in a three-dimensional lock-exchange system. *Ocean Model.* 26, 134–155.
- Pacanowski, R. C., Gnanadesikan, A., 1998. Transient Response in a Z-Level Ocean Model That Resolves Topography with Partial Cells. *Monthly Weather Review* 126, 3248–3270.
- Prather, M., 1986. Numerical advection by conservation of second-order moments. *J. Geophys. Res.* 91, 6671–6681.
- Shchepetkin, A. F., McWilliams, J. C., 1998. Quasi-monotone advection schemes based on explicit locally adaptive dissipation. *Mon. Wea. Rev.* 126, 1541–1580.
- Shchepetkin, A. F., McWilliams, J. C., 2005. The regional oceanic modeling system (roms): a split-explicit, free-surface, topography-following-coordinate oceanic model. *Ocean Model.* 9, 347–404.
- Simmons, H. L., Jayne, S. R., St-Laurent, L. C., Weaver, A. J., 2004. Tidally driven mixing in a numerical model of the ocean general circulation 6, 245–263.
- Smagorinsky, J., 1963. General circulation experiments with the primitive equations: I. The basic experiment. *Mon. Wea. Rev.* 91, 99–164.
- Smagorinsky, J., 1993. Some historical remarks on the use of nonlinear viscosities. In: Galperin, B., Orszag, S. A. (Eds.), *Large Eddy Simulation of Complex Engineering and Geophysical Flows*. Cambridge University Press, pp. 3–36.
- Stacey, M. W., Pond, S., Nowak, Z. P., 1995. A numerical model of the circulation in Knight Inlet, British Columbia, Canada 25, 1037–1062.
- Tatebe, H., Hasumi, H., 2010. Formation mechanism of the pacific equatorial thermocline revealed by a general circulation model with a high accuracy tracer advection scheme. *Ocean Modelling* 35, 245–252.
- Winters, K. B., Lombard, P. N., Riley, J. J., D’Asaro, E. A., Apr. 1995. Available potential energy and mixing in density-stratified fluids. *Journal of Fluid Mechanics* 289, 115–128.
- Winton, M., Hallberg, R., Gnanadesikan, A., Nov. 1998. Simulation of Density-Driven Frictional Downslope Flow in Z-Coordinate Ocean Models. *Journal of Physical Oceanography* 28, 2163–2174.
- Wunsch, C., Ferrari, R., 2004. Vertical mixing, energy, and the general circulation of the ocean. *Annual Reviews of Fluid Mechanics* 36, 281–314.